Background and Lunar Neutron Populations Detected by LEND and Average Concentration of Near-Surface Hydrogen Near the Moon's Poles

T. A. Livengood, *CRESST/University of Maryland at Planetary Systems Laboratory, NASA Goddard Space Flight Center, Greenbelt, MD 20771*

I. G. Mitrofanov, *Institute for Space Research, Moscow, Russia*

G. Chin, *NASA Goddard Space Flight Center, Planetary Systems Laboratory, Greenbelt, MD 20771*

W. V. Boynton, *University of Arizona, Lunar and Planetary Laboratory, Tucson, AZ*

J. G. Bodnarik, *University of Arizona, Lunar and Planetary Laboratory, Tucson, AZ*

L. G. Evans, *Computer Sciences Corporation, Lanham-Seabrook, MD 20706*

K. P. Harshman, *University of Arizona, Lunar and Planetary Laboratory, Tucson, AZ*

M. L. Litvak, *Institute for Space Research, Moscow, Russia*

T. P. McClanahan, *NASA Goddard Space Flight Center, Planetary Systems Laboratory, Greenbelt, MD 20771*

R. Z. Sagdeev, *Department of Physics, University of Maryland, College Park, MD 20742*

A. B. Sanin, *Institute for Space Research, Moscow, Russia*

R. D. Starr, *Department of Physics, Catholic University of America, Washington, DC 20064*

J. J. Su, *Department of Physics, University of Maryland, College Park, MD 20742*

Running Title:	Lunar neutrons detected by LEND
Tables:	6
Figures:	6
Supplemental:	1 file

Correspondence to: Dr. Timothy A. Livengood
Code 693
NASA Goddard Space Flight Center
Greenbelt, MD 20771

E-mail: timothy.a.livengood@nasa.gov
Telephone: 301-286-1552
Fax: 301-286-1683

Abstract:

Neutron flux measurements by the Lunar Exploration Neutron Detector (LEND) on the Lunar Reconnaissance Orbiter (LRO) enable quantifying hydrogen-bearing volatiles in the lunar surface from orbit. Accurately determining hydrogen abundance requires discriminating between the instrument background detection rate and the population of lunar-sourced neutrons that are sensitive to surficial hydrogen. We have investigated the detection rate for lunar and non-lunar (spacecraft-sourced) neutrons in LEND by modeling maps of measured count rate in three LEND detector systems using linear combinations of maps compiled from LEND detectors and from the Lunar Prospector Neutron Spectrometer. We find that 30% of the global-average 24.926±0.020 neutron counts per second (cps) detected by the LEND STN3 thermal-energy neutron sensor are lunar-sourced neutrons in the thermal energy range (E<0.4 eV), 65% are lunar-sourced neutrons in the epithermal and fast energy range (E>0.4 eV), and 5% are from spacecraft-sourced background signal. In the SETN epithermal neutron detector, 90% of the 10.622±0.002 neutron detections per second are consistent with a lunar source of epithermal and fast neutrons combined (E>0.4 eV), with 3% due to lunar-sourced thermal neutron leakage into the detector (E<0.4 eV), and background signal accounting for 7% of total detections. Background signal due to spacecraft-derived neutrons is substantial in the CSETN collimated detector system, accounting for 57% of the global average detection rate of 5.082±0.001 cps, greater than the 48% estimated from cruise-phase data. Lunar-sourced epithermal and fast neutrons account for 43% of detected neutrons, including neutrons in collimation as well as neutrons that penetrate the collimator wall to reach the detector. We estimate a lower limit of 17% of lunar-sourced neutrons detected by CSETN are epithermal neutrons in collimation (0.37 cps), with an upper limit estimate of 54±11% of lunar-sourced neutrons received in collimation, or 1.2±0.2 cps global average. The pole-to-equator contrast ratio in epithermal and high-energy epithermal neutron flux indicates that the average concentration of hydrogen in the polar regolith above 80° north or south latitude is ~105 ppmw (parts per million by weight), or 0.095±0.01 wt% water-equivalent hydrogen. Above 88° north or south, the concentration increases to ~140 ppmw, or 0.13±0.02 wt% water-equivalent hydrogen. The similar pattern of neutron flux suppression at both poles suggests that hydrogen concentration generally increases nearer the pole and is not closely associated with a specific feature such as Shackleton Crater at the lunar south pole that has no northern counterpart. Epithermal neutron flux decreases with increasing latitude outside the polar regions, consistent with surface hydration that increases with latitude if that hydration extends to ~13–40 cm into the surface.

Introduction

The flux of neutrons from solid surfaces exposed to galactic cosmic rays (GCR) can be measured by spacecraft instrumentation to explore composition of the upper regolith (~1m) in planetary bodies. Neutron remote sensing poses technical challenges in that neutrons are not focused effectively with current technologies, and a significant background flux of neutrons is formed by GCR impacts on spacecraft structures local to the detector. The Lunar Exploration Neutron Detector (LEND) on the Lunar Reconnaissance Orbiter (LRO) spacecraft addresses the challenge of directing neutrons by placing a subset of its detectors within a collimator structure that reduces the population of neutrons that reach the detector from outside a limited range of acceptance angle (Mitrofanov *et al.* 2010a). The detectors within the collimator structure receive background neutron flux from the surrounding structure, and LEND also has uncollimated detectors mounted on the outside of the collimator structure which receive background neutron flux generated within the body of the spacecraft and the neighboring collimator. The relatively high mass of the collimator prevented deploying LEND on a boom and thus LEND was mounted to the spacecraft body, which maximizes the solid angle subtended by the spacecraft neutron source. Neutron remote sensing detects hydrogen and other species by their suppression of neutron flux. Localized deposits of these species can be identified even in raw flux measurements, but accurate quantitative measurements require determining and subtracting the background.

Data acquired at the Moon during the first (roughly) two and a half years of the LRO mission demonstrate the actual performance of the LEND instrument in action at the Moon, responding to the combined lunar neutron flux and background. This work tests background estimates in three of LEND's detector systems that were determined from cruise-phase measurements en route to the Moon (Litvak *et al.* 2012a) and uses a method independent from a recent determination of background detection rates by Litvak *et al.* (2016). The present method also explores similarities and differences between measurements of neutron flux by LEND and by the earlier Lunar Prospector (LP) neutron detectors (Feldman *et al.* 1999). All of the data used here were downloaded from the Planetary Data System Geosciences Node, hosted by Washington University in St. Louis (http://geo.pds.nasa.gov) and thus are freely available to the lunar science community to test the conclusions of this work.

The primary task for LEND is to map the distribution and magnitude of suppression in the Moon's neutron flux as an indicator for the presence of hydrogen, and thus water, in the upper meter of the regolith near the poles. Hydrogen, as water, is expected to be concentrated within permanently shadowed regions (PSRs) near the lunar poles (Watson *et al.* 1961; Carruba and Coradini 1999). Hydrogen or water may come from the constant influx of solar wind, from impacts by hydrated micrometeoroids, from pulsed delivery of water and other volatiles by major cometary or asteroidal impacts, or from outgassing volatiles from the lunar interior. Remote detections of mineral hydration in the Moon's

near-infrared reflectance spectrum show that water or hydroxyl is more widely distributed than expected (Sunshine *et al.* 2009; Pieters *et al.* 2009; Clark 2009; Livengood *et al.* 2011), expanding the range of regions on the Moon whose hydrogen content is important to understand. Understanding the background detection rate in LEND is necessary to measure small quantities of water that are widespread.

Neutron remote sensing measures the quantity of hydrogen in the regolith through a local deficit in the flux of epithermal neutrons (~0.4 eV < E < ~100 keV) that are created by galactic cosmic ray (GCR) spallation from atomic nuclei in the Moon (Boynton *et al.* 2012). A deficit in the epithermal neutron leakage flux is caused by collisions with hydrogen atoms, which efficiently degrade neutron energy below the threshold of the thermal range (E<~0.4 eV). For modest hydrogen concentrations up to a few thousand parts per million by weight (ppmw) or a few percent or less of water-equivalent hydrogen by weight (wt% WEH), the fractional abundance of hydrogen is directly proportional to the fractional deficit of epithermal neutrons relative to unsuppressed neutron leakage from a hydrogen-poor reference region of similar mineralogy (see Eqn. 8). If the detector background were not subtracted, the measurement would underestimate the actual hydrogen concentration, resulting in a hard lower limit on the abundance of hydrogen in the regolith.

LEND is the second orbital neutron detection instrument deployed at the Moon to investigate the quantity and spatial distribution of hydrogen in the lunar surface, enlarging on results from Lunar Prospector (Hubbard *et al.* 1998). The LP investigation of water deposits in the Moon's polar regions was reported by Feldman *et al.* (2000; 2001; 2004). The Lunar Prospector mission was terminated by intentional lunar impact on 31 July 1999 (Goldstein *et al.* 1999). Lunar Prospector operated in two phases, initially at 100 km altitude and later at 30 km altitude. The spatial footprint of omnidirectional neutron detectors, such as used on LP, is proportional to altitude. We use data from the low altitude phase of the LP mission to compare with LEND measurements at ~51 km altitude.

The present work models the spatial distribution of lunar neutron flux measured by three of the LEND detectors, using comparable data from LP as well as using LEND data to compare between detector systems (Fig. 1). This effort differs from Litvak *et al.* (2012b), which compares the first 1.3 years of LEND data to LP mapped neutron flux measurements, by using substantially more LEND data and by quantitatively investigating the relative contribution of neutrons from different populations in each LEND detector. Litvak *et al.* (2016) also investigated LEND detector background, using orbital phase profiles rather than complete two-dimensional maps and using only data from LEND detectors rather than LP. Eke *et al.* (2012) modeled the performance of one LEND detector system, the CSETN collimated detector, comparing the data stream of individual one-second integrations by LEND against latitude-longitude maps compiled from LP. The present effort differs from Eke *et al.* (2012) by comparing maps assembled by comparable methods for LEND and LP both, and by investigating two other LEND detector systems as well as CSETN. The

compiled LEND maps are assembled from data reduced, calibrated, and flagged by LEND standard processing for Derived LEND Data products (DLD) for the PDS (Litvak *et al.* 2012a). An ASCII text file recording the mapped LEND data and detector backgrounds derived from this work can be found in the online Supplemental Materials.

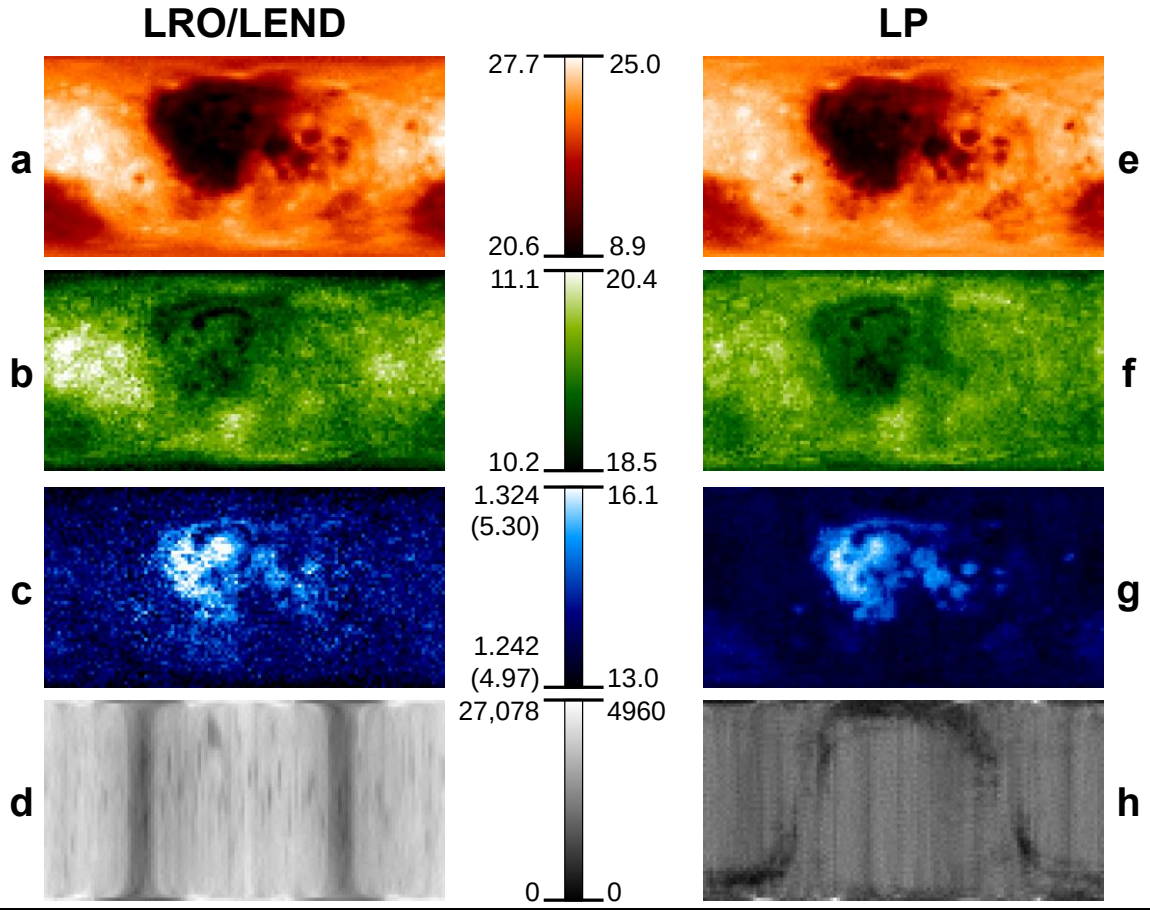

Fig. 1: Lunar neutron flux mapped by LEND (*a, b, c*) and by LP (*e, f, g*) with 3° square pixels over the full range of latitude (±90°) and longitude (±180°). Neutron detection rates stretch between minimum (dark) and maximum (bright) as shown by the respective color scales for each image set, labeled in counts per second. LEND detectors are (*a*) STN3; (*b*) SETN; and (*c*) CSETN. Maps displayed for LP are: (*e*) thermal neutrons; (*f*) epithermal neutrons; (*g*) fast neutrons. Integration time per map pixel is shown for the CSETN detector (*d*; 7788–27078 sec) and for LP (*h*; 256–4960 sec). Count rates for the CSETN detector are labeled by count rate per detector, as well as the 4-detector equivalent count rate, in parentheses.

In the following section, we summarize relevant features of LEND and its major differences from the LP neutron detectors and discuss constructing maps using both LP and LEND data. We show how archived data from LP can be used to estimate contributions to the LEND detectors from lunar and non-lunar sources and to estimate parameters

required to reduce LEND data and eliminate background and out-of-band contributions in the different detectors. Finally, we address distinctions between neutron flux measured by LEND and neutron flux measured by LP, including both the uncollimated and the collimated LEND detectors. We identify a persistent discrepancy in the polar regions between two of the LP neutron flux maps in comparison to corresponding LEND measurements and argue that this discrepancy is an artifact of the LP data that is not present in the LEND detectors nor in the remaining one of the three LP neutron detector systems. The ratio between the epithermal neutron flux at the relatively dry equator and at the poles yields estimates for the regionally averaged hydrogen content in the polar regolith.

Instruments and Data Reduction

The Lunar Reconnaissance Orbiter was launched 18 June 2009 and entered the mapping phase of its mission on 15 September 2009 in a circular polar orbit of the Moon at approximately 51 km altitude (average of actual data collection), covering the entire lunar surface in both day and night phases in one lunation. The spacecraft was moved to a dynamically stable elliptical orbit in December 2011, to conserve fuel and maintain operational capability for as long as possible during the extended mission (Vondrak *et al.* 2012). LEND measurements used for the present work were collected between 16 September 2009 and 31 December 2011, restricted to data collected in the altitude range 51±15 km, which includes more than 80% of data, distributed approximately symmetrically about the mean value. Limiting to data prior to 2012 enables multiple detector systems to be considered contemporaneously, since an instrument anomaly in May 2011 ended useful data from two of the detectors that we consider here, STN3 and SETN. The anomaly appears to have been an electrical discharge (arcing) within high-voltage circuitry that damaged an electronics board that digitized the signal from some detectors, including SETN. The STN3 detector and one element of the CSETN collimated detector shared the responsible high-voltage electronics, which have been switched off to protect the rest of the instrument. There have been no subsequent anomalies that resulted in reducing instrument function.

LEND is body-mounted on the 3-axis stabilized polar-orbiting LRO spacecraft. The configuration of LEND is described and illustrated by Mitrofanov *et al.* (2010a). Eight of the LEND detectors are functionally identical cylindrical ^{3}He-filled proportional counters, differing in terms of cladding and mounting position. The LEND high-energy neutron detector SHEN, which is not used in this work, employs a stilbene scintillator with anti-coincidence shield and is the only LEND detector that is not a gas proportional counter. The detectors are mounted with long axis parallel to each other and aligned towards the z-axis of the LRO spacecraft, normally the nadir direction. All LEND measurements that are used here were acquired within 2° of nadir pointing, for stable observational geometry. Detected neutrons include lunar sources as well as neutrons from GCR spallation off of spacecraft and instrument components.

Standard LEND data-processing methods are described by Litvak *et al.* (2012a). LEND data used here were obtained from the PDS in the calibrated DLD (Derived LEND Data) format, which is derived from Reduced Data Records (RDR) files, which also are available on the PDS. The full set of quantitative calibration steps applied in creating the RDR and DLD data sets are described by Litvak *et al.* (2012a) and by Boynton *et al.* (2012). Each record in the DLD format corresponds to a single 1-second integration of neutron detection events for all operating detectors in the LEND instrument and includes spacecraft event time, calendar date and time, local solar time, lunar latitude and longitude, the number of counts in each LEND detector, and estimated background in each detector. Altitude information was recovered from spacecraft ephemerides. The background recorded in the DLD was estimated from data collected during the short cruise to the Moon, in the absence of lunar neutrons; this background is tested by the present work. LEND acquires up to 86,400 records in a terrestrial day to make one DLD file. This work uses 771 DLD files, although not every file covers a complete day, due to spacecraft events such as pointing off-nadir for the benefit of other LRO measurements, conflict with charged particle flux from solar particle events, or instrument or spacecraft anomalies. No DLD records are produced for periods in which the instrument was switched off.

In the maps constructed from the data used in this work, mean altitude as a function of latitude varies from a minimum of 48.0 km at the north pole to a maximum of 52.8 km at the south pole. Over this altitude range, the detector background due to GCR impinging on the spacecraft is expected to vary by 0.86% due to the change in solid angle subtended by the Moon that occults the otherwise isotropic cosmic ray fluence (Litvak *et al.* 2012a). Treating the background as a spatially uniform component of the total neutron detection rate thus is likely to overestimate the background at the low altitude of the north pole by ~0.43%, and underestimate the background at the high altitude of the south pole by ~0.43%. This is small compared to the uncertainties that are derived for the background (below). The altitude also varies as a function of longitude, from a minimum of 43.0 km altitude at ~15°N on the lunar nearside, to a maximum of 58.1 km altitude at ~15°S on the lunar farside, with the background varying by 2.8% between the nearside minimum and the farside maximum. The variability of the background with altitude is opposed by variability in the flux of lunar neutrons, which decreases with altitude so that the magnitude of variation in the total signal is less than the variation in either component. Eke *et al.* (2012) constructed an empirical distribution of signal versus altitude for the LEND detector CSETN which shows that the total signal declines by about 1.1% with altitude increasing from 40 km to 60 km. Since the GCR-induced background increases with altitude, the lunar-sourced neutron flux must decrease by more than the background increases. Since the two effects are close to balance over the relatively narrow altitude range from which data are drawn for this work, the overestimate of background at altitudes below the 51 km average mostly compensates for the underestimate of lunar neutrons, and vice-versa. The empirical deviation in the magnitude of CSETN total signal due to variations of spacecraft

altitude with respect to the 51 km mean altitude are thus of order ±1.1%•((58.1-43.0)/20)/2 = ±0.42% of the CSETN total signal, which is approximately a factor of two greater than the background estimated below. The estimated uncertainty in the CSETN background is about ten times this altitude variability, which is thus not important to the outcome. Variation with altitude of signal from the uncollimated LEND detectors, in which the background component is much smaller and the lunar signal varies substantially with altitude, is corrected as part of the standard processing described by Litvak *et al.* (2012a).

The LEND proportional-counter detectors are switched off while operating the LRO rocket motor for station-keeping maneuvers due to arcing in the high-voltage electronics caused by exhaust gases. Station-keeping was conducted approximately every two weeks during the circular-orbit phase of the mission, when the normal to the spacecraft orbit plane was aligned with the Earth-Moon axis so that the spacecraft could communicate with the ground station at all times in case of trouble. Maneuvers thus took place when the spacecraft orbit was near longitudes ±90°, over a variety of local time values, resulting in reduced integration time at these longitudes (Fig. 1). LRO orbital period is less than two hours; as a result, any uncalibrated variations in detector sensitivity, variations in GCR flux, or effects due to detector inactivity that last significantly longer than two hours, would appear in mapped LEND data as striping nearly parallel to longitude, affecting all latitudes equally. Figure 1 reflects the reduced net integration time and resulting signal-to-noise ratio at longitude ±90°.

Variations in the sensitivity of individual detectors and in the GCR flux that produces lunar neutrons and spacecraft-generated (background) neutrons are compensated in routine data reduction. Detector sensitivity increases over a period of a few weeks after switch-on, approaching ~27% greater sensitivity than at switch-on in the example shown by Litvak *et al.* (2012a). Similar sensitivity variation occurs in all the LEND ^{3}He-detectors and appears consistent with surface charging on the insulated stand-off that supports the central electrode within the detector chamber, increasing the active length of the detector by about the same proportion. The variation in sensitivity is modeled as an exponential function, appropriate to the behavior of a resistive-capacitive circuit. Sensitivity in each individual LEND detector is calibrated independently using data acquired from a narrow range of latitude around each lunar pole, representing a repeatable measurement of neutron flux (Litvak *et al.* 2012a; Boynton *et al.* 2012). Calibrating by this standard corrects for any long-term change in detector sensitivity, as well as variability in the lunar neutron leakage flux. Since lunar neutrons arise from GCR interactions with the lunar regolith, and background neutrons also arise from GCR interactions with spacecraft materials, the total signal in the detector scales uniformly with changes in GCR flux.

Lunar Prospector was in polar orbit, spin-stabilized with rotation axis nearly parallel to the Moon's rotation axis (Binder 1998). Two of the LP neutron detectors were mounted on a 2.5m-long boom extended perpendicular to the spin axis, with the two ^{3}He-filled

cylindrical proportional-counter detectors for thermal and epithermal neutrons mounted end-to-end, oriented perpendicular to the boom and perpendicular to the spacecraft spin axis (Maurice *et al.* 2004). Measurements from these detectors were corrected for the detector cross-section presented to the lunar surface, as the detectors were parallel to the surface over the poles and continuously alternated between perpendicular and parallel to the surface over the equator due to spacecraft rotation. A small background component of neutron flux was generated from GCR impacts on spacecraft hardware, relatively little due to the detectors' position on the boom, separated from the bulk of the spacecraft. A third neutron energy range, fast neutrons, was detected with the anti-coincidence shield (ACS) of the Lunar Prospector gamma ray spectrometer, mounted on a different boom. The ACS used a borated plastic scintillator and photomultiplier detectors to detect neutron capture events. The ACS was shaped as a cup surrounding the gamma ray scintillator component, with a stubby cylindrical base of approximately equal height and diameter. Signal in the ACS varied with the geometry of the detector relative to the lunar surface, which was parameterized and corrected by Maurice *et al.* (2000) as a function of latitude using measured count rates obtained over the lunar highlands. Data reduction and calibration procedures for the LP neutron detectors are described by Maurice *et al.* (2004). The LP neutron flux data products available from the PDS have already had background-subtraction and geometrical corrections performed.

A neutron-detection event in the LEND proportional counter detectors occurs when a neutron penetrates into the detector chamber to be captured by a ^{3}He nucleus, forming a triton and a free proton and releasing an electron and 764 keV of binding energy as the total kinetic energy of the products. Collisions of the energetic products with the remaining ^{3}He gas results in ionization proportional to the release of energy, generating a pulse of current between a central electrode and the chamber wall that is proportional to the energy. Neutron-detection events are distinguishable from the continuum of pulse magnitude created by charged particles, which also may be detected but with an energy spectrum that peaks at low energy (Litvak *et al.* 2012a). Measured signal is the count of neutron-detection events within 1-second integration intervals. The triton eventually undergoes a beta-decay to ^{3}He, leaving a net increase of one hydrogen atom in the detector chamber. Detection efficiency degrades for neutrons entering the chamber with energy greater than ~1 eV and is near zero for energy greater than ~10 keV (Litvak *et al.* 2012a).

The three LEND detector systems investigated here are:

1. STN3 – uncollimated Sensor for Thermal Neutrons. This detector is mounted outside the LEND collimator structure and near its nadir-pointed apex so that it receives lunar neutrons from all directions and all energies. The identical STN1 and STN2 detectors are mounted fore-and-aft on the outside base of the collimator so that one is exposed primarily to neutrons from the direction of travel along the orbit and the other is exposed to neutrons from the trailing direction. STN3 is positioned

such that it is unaffected by the velocity of the spacecraft, which has a significant influence on detection rates for low-energy thermal neutrons detected by STN1 and STN2. The globally averaged count rate in the STN3 detector is 24.93±0.02 counts per second (cps).

2. SETN – uncollimated Sensor for EpiThermal Neutrons. This detector is mounted similarly to STN3, on the opposite side of the collimator structure. It differs from STN3 in that it is wrapped in cadmium foil, which has a high absorption cross-section for neutrons of energy less than ~0.4 eV, so that SETN accepts neutrons only of greater energy. The LP epithermal-neutron detector also used cadmium foil to exclude thermal neutrons from detection. The globally averaged count rate in the SETN detector is 10.622±0.002 cps.
3. CSETN – Collimated Sensor(s) for EpiThermal Neutrons. The signal from the CSETN detector system is collected from up to four detectors located within a collimator structure. The collimator design is an aluminum structure that encases polyethylene beads and an inner shield containing ^{10}B. The hydrogen-rich polyethylene moderates the energy of neutrons that enter the walls of the collimator so that they have a high probability of capture by the ^{10}B. Each detector sits at the base of an open barrel in the collimator, positioned so that the long axis of the detector and of the open barrel point in the direction of the LRO spacecraft z-axis, the nadir direction in normal operation, with the field of view defined by the barrel opening. A cadmium window in the barrel absorbs low-energy neutrons so that only epithermal neutrons are detected in collimation. Neutrons that reach the detector in collimation will have approximately the same energy spectrum as those detected by the uncollimated SETN detector. Lunar neutrons that reach the detector out of collimation must penetrate the collimator wall and must have greater initial energy in order to reach the detector even after moderation by the polyethylene and potential capture by the ^{10}B. The mean energy of the total lunar neutron population detected by CSETN thus skews toward higher energy epithermal neutrons, or HEE neutrons as labeled by Eke *et al.* (2012) and by Lawrence *et al.* (2011a). The globally averaged count rate in the CSETN detectors is 1.2705±0.0003 cps per detector, or 5.082±0.001 cps total.

The STN3 and SETN detectors are corrected for altitude-dependence in measured lunar flux and spacecraft-sourced neutron production due to variations in the Moon's shadowing of GCR fluence at the spacecraft. We test alternative detector background at the LRO mean altitude but make no attempt to replace or supersede the rest of the reduction scheme described by Litvak *et al.* (2012a). No altitude-dependent correction is applied to CSETN data in the standard data reduction.

Neutron emissions mapped by LEND were shown by Litvak *et al.* (2012b) to be qualitatively similar to results from LP, a decade earlier (Fig. 1). The neutron spectrum

reflects geochemistry, resulting in regional variability of the neutron flux in the energy intervals sensed by both LEND and LP (Lawrence *et al.* 2006). A map of the LEND STN3 signal qualitatively resembles thermal neutron flux measured by LP, as expected. A map of the SETN signal qualitatively resembles epithermal neutron flux measured by LP, as expected. A map of the CSETN signal qualitatively resembles fast neutron flux measured by LP, consistent with a fraction of neutrons detected by CSETN including greater initial energy to penetrate the collimator and reach the CSETN detectors out of collimation (e.g., Mitrofanov *et al.* 2011; Lawrence *et al.* 2011a). The distinctive morphology of neutron emissions in the LP and LEND data sets provides a means to distinguish contributions to the LEND signal from neutrons in energetically distinct populations measured by LP.

Constructing Maps

Cylindrical-projection maps of neutron detection rate can be constructed in a straightforward fashion, by summing detected counts of every 1-second measurement that fall within bins of chosen angular dimension in spacecraft latitude and longitude, divided by total integration time within that bin. Polar orbit means that the latitude and longitude of the spacecraft both vary linearly with time, so that integration time and statistical uncertainty are distributed evenly across a cylindrical projection map (Fig. 1d&h), in contrast to equal-area projection (*e.g.*, Eke *et al.* 2012), which concentrates integration time per unit surface area in the polar regions. The map construction that is employed here provides a natural way to handle times when one or two of the CSETN detectors were powered off, by separately totaling counts and integration time for each of the detectors to obtain an average signal per detector that can be multiplied by four to yield the equivalent of the combined CSETN count rate with all four detectors in operation, the standard way that CSETN data have been presented. The mapped net integration time is minimum, and statistical uncertainties somewhat greater, at longitude ±90°, as expected due to station-keeping (Fig. 1).

LP neutron flux measurements are reported in the PDS data sets in units of counts per 8-second or per 32-second interval, but otherwise can be handled similarly to the LEND data, dividing total counts within a latitude-longitude cell by total dwell time in that cell to yield counts per second. Only the LP data collected with the longer integration time includes fast-neutron data, thus we use only the 32-second data. The band of minimum integration time for LP neutron measurements is not quite parallel to lines of longitude, as it is for LEND, but integration time and thus statistical significance are otherwise spread fairly evenly over the Moon (Fig. 1).

The mapped quantity is count rate at the spacecraft, comprising the uniform background of spacecraft-sourced neutrons plus a quantity proportional to the flux of lunar neutrons while in that position. We do not apply any smoothing to these maps, as the stochastic noise of the individually-measured map cells is essential to evaluate goodness-of-fit and to

discriminate between models of the mapped data. This aspect of map construction differs significantly from maps constructed by Litvak *et al.* (2012b) and by Maurice *et al.* (2004), who smooth their maps to reduce noise and to reveal the distribution of neutron emission rate at the resolution of the omnidirectional detectors. Although each measurement is in response to neutrons emitted from a broad field of view over the lunar surface, the actual measured counts (and noise) found within a given bin of the unsmoothed map belong to instances when the spacecraft could be found within that latitude-longitude bin.

The choice of angular dimension for the map binning is significant. The LEND CSETN detection system is designed to obtain relatively high spatial resolution on the component of signal that reaches the detectors through the barrel of the collimator, with finer resolution than the LP neutron flux measurements. LP flux maps have finer resolution than the omnidirectional detectors of LEND, since LP operated closer to the lunar surface (~30 km altitude) while obtaining the data used here; on the other hand, the 32-second integration time means that the spacecraft traveled 1.6° in latitude during each sample compared to 0.05° for LRO and LEND. Any element of fine spatial resolution that is present in mapping one data set, but not the other, resembles noise and skews the outcome of a least-squares goodness-of-fit minimization in constructing a model for LEND maps using LP mapped data. We consider this to be a significant difference between the present work and work by Eke *et al.* (2012), which compared individual one-second integrations with maps derived from LP data, mismatching fine-scale properties between the two data sets.

We choose a binning dimension, 3°×3°, broad enough that the estimated field of view (FOV) of both the LEND and LP omnidirectional detectors is contained within one element in the direction of travel. A comparison between LEND and LP can be based on regionally variable flux measurements that the two systems should have in common, rather than localized flux measurements that would emphasize their differing properties. The effective FOV cited for the LP neutron detectors is of order 45 km (Maurice *et al.* 2004), which projects to 1.5° in latitude and longitude at the equator. LEND operates at higher altitude and so its omnidirectional detectors are sensitive to a proportionately broader field of view, 45•51/30 = 76.5 km, which projects to 2.5° in latitude and longitude at the equator. We choose a somewhat broader binning scale of 3°; tests with 4° and 5° binning yield the same qualitative results as the 3° binning.

All maps and models displayed in this work use 3° binning and 7200 sample elements to cover the full range in latitude and longitude. At this sampling scale, the information content in LEND and LP maps of lunar neutron flux should differ only in the measurement uncertainty and any systematic artifacts such as detector background ('dark') signal. Neither data set should retain the underlying spatial variation of the measured signal at fine resolution. The maps of LEND total neutron-detection counts, total integration time in each detector, and estimated background and out-of-band contribution compiled for 3° binning are reported in an ASCII text file in the online Supplemental Materials.

Modeling LEND Maps

We model each map of LEND detector signal using a linear combination of a uniform signal for spacecraft background and templates derived from the LP thermal, epithermal, and fast neutron maps. It is evident by inspection of Fig. 1 that the mapped LEND signal in the STN3 (nominally thermal), SETN (nominally epithermal), and CSETN (collimated epithermal) detectors is patterned similarly to the thermal, epithermal, and fast neutron maps from LP, respectively. Background already has been subtracted from the LP neutron data as furnished through the PDS. Litvak *et al.* (2012b) demonstrate the similarity between LEND and LP mapped data by plotting the LEND measurements against LP neutron flux measurements in corresponding mapped locations to demonstrate the correlation between the LEND uncollimated detectors and their LP counterparts.

The templates consist of each of the LP neutron flux maps normalized to its average value, resulting in a surface of approximately unity value, with the unique spatial modulation that corresponds to each neutron energy range. Coefficients applied to the templates are in units of counts per second (cps) and represent the globally averaged contribution to each LEND detector that is due to neutrons in each mapped source population. The geographically averaged mean count rate in each of the LEND detector systems, STN3 (24.93±0.02 cps), SETN (10.622±0.002 cps), and CSETN (5.082±0.001 cps), is reported in Table 1. The mean count rate for each detector is estimated by averaging the measured count rate per pixel across the map, estimating the precision uncertainty as standard error of the mean. The count rate and uncertainty estimated from Poisson statistics by totaling all counts and dividing by the total of all integration time yields nearly the same result and uncertainty as the geographic average, but that is an average over time rather than an average over geography.

Table 1 reports the best-fit coefficients from modeling the LEND detectors with linear combinations of LP map templates, with uncertainties; the methodology is described in greater detail below. All three LEND detectors appear to be sensitive to lunar epithermal and fast-neutron populations despite the fact that ^{3}He detectors have no significant sensitivity at energies greater than 10 keV. The uncollimated epithermal-neutron detector, SETN, has a small sensitivity to thermal neutrons, while the collimated detector, CSETN, has no sensitivity to thermal-energy neutrons. SETN has the least relative sensitivity to fast neutrons, while CSETN displays the greatest relative sensitivity to fast neutrons, consistent with expectation that the total detection rate in CSETN skews toward HEE neutrons (high energy epithermal). The collimator adjacent to (or surrounding) the detectors can moderate the energy of lunar neutrons while scattering them to the detectors, thereby rendering the high-energy population detectable. The actual energy distribution in the population of detected neutrons that leave the Moon with energy greater than 10 keV is not determined; they may not actually be "fast" neutrons (E>1 MeV) but a moderate-energy population that is spatially distributed similar to the fast neutron population. Several analyses support the

detectability by CSETN of a moderate energy population of neutrons in the 10 keV to 1 MeV energy range (Eke *et al.* 2012; Lawrence *et al.* 2011a; Litvak *et al.* 2011). Experiments with using a template from LEND's own fast neutron detector in the same role as the fast neutron map from LP have resulted in substantially greater residuals in the fit. The sensitivity of the stilbene-based LEND fast neutron detector SHEN (Sensor for High Energy Neutrons; Mitrofanov *et al.* 2010a) is limited to 1-6 MeV neutrons. The fast neutron detector on LP also is nominally limited to neutrons of energy >1 MeV. However, McElhaney *et al.* (1990) have shown that the BC-454 scintillant used in the LPGRS anti-coincidence shield/fast neutron detector (Feldman *et al.* 1999) also is sensitive to neutrons of energy 100–1000 keV in the laboratory, and Feldman *et al.* (1998a) note that the sensitivity of the ACS in Lunar Prospector favored the low-energy end of the fast neutron distribution. Greater sensitivity to the moderate-energy population of neutrons may account for the fact that the LP fast neutron map yields a better model for the LEND maps than SHEN.

The method to identify best-fit coefficients for the LP-derived templates and to estimate uncertainties in modeling the LEND maps must accommodate substantial covariance in the coefficients, since the templates are not mathematically orthogonal. Each parameter set includes up to four coefficients, one for each of the three LP-derived map templates (thermal, epithermal, and fast neutrons) and one for a geographically uniform signal contribution due to spacecraft-sourced neutrons. We have adopted an evolutionary algorithm in which successive generations of a few tens of thousands of randomly-selected parameter sets are used as coefficients to model each LEND map, ultimately resulting in testing a few hundred thousand to a million distinct parameter sets in each fitting operation, with the constraint that all coefficients in each trial must be greater than or equal to zero. The best-fitting model in each successive generation is identified by a least-squared deviation criterion and is used as the central value for the next generation of parameters. The breadth of parameter space that is explored by random selection in successive generations is expanded or contracted for each coefficient depending on whether the "best fit" value for that parameter is near the edge of the tested range in each generation or near the central value. The procedure is repeated until converging on a best-fit set of coefficients in consecutive generations, retaining all the tested parameter sets to investigate uncertainties. We have tested various initialization schemes for parameter central values and parameter randomization, including both realistic values near previous best-fit parameter sets as well as unrealistic values that start far from any plausible parameter set, with broad ranges of random selection. The best-fit results are repeatable, with small variability within the range of the estimated uncertainties due to the discrete nature of the parameter-generation method. The initial breadth of the random parameter distribution is selected to be at least wide enough to ensure that the population of random parameter sets is well populated far from the best-fit value, to enable a well-characterized fit uncertainty on each parameter.

Uncertainty in the coefficients is estimated using the Fisher *F* statistic formed from a ratio of variances. The statistical variance (sum of squared deviations) between each tested model and the LEND map is compared to the variance between the best-fit model and the LEND map to test for models that are indistinguishable at less than the 1σ (68.27%) confidence level in a model with N = (360/3)*(180/3) - 4 = 7,196 degrees of freedom, computing the limiting value of *F* using code adapted from Press *et al.* (1989). The maximum difference in each coefficient between the best-fit value and its value in all parameter sets that meet the limiting criterion in *F* is adopted as the 1σ uncertainty of each coefficient. This is a conservative uncertainty estimate that does not assume prior knowledge of the statistical properties of the LEND measurements and that tolerates comparing an imperfect best-fit model with other models that are even more imperfect. This algorithm naturally incorporates covariance between all model parameters since it explores the entire range of tested models that fit the statistical criterion.

Analysis of LEND STN3 detector: The coefficient for the uniform component of neutrons detected by STN3 is required to be no less than zero, as a negative particle-detection rate has no physical meaning, resulting in a background of 0±1.0 counts per second (cps); really, a 1σ upper limit of 1.0. The coefficient of the LP thermal-neutron template is 8.4±0.4 cps out of a mean STN3 count rate of 24.93±0.02 cps, accounting for 34±2% of signal in this detector. The remaining signal is a combination of neutrons originating in the epithermal population, 49±5% of the total, and in the fast-neutron population, accounting for 17±4% of the total. Combined, the epithermal and fast neutrons account for 16.5±1.1 cps, or 66±4% of the total signal.

The best-fit model map is nearly indistinguishable from the LEND map of Fig. 1a under visual inspection and thus is not displayed. Instead, Fig. 2a plots the modeled value against the measured value of each STN3 pixel. The dispersion in values in each of the plotted axes corresponds to modeling defects and measurement noise in the data and the component templates. The dispersion is not symmetric about a line of slope unity that represents perfect correlation, indicating systematic discrepancies between the model and data. Figure 2a includes a smoothed map of absolute magnitude of the residuals between the model and the data, showing that there are, indeed, systematic regional discrepancies between the LEND map and a model based on LP neutron flux maps. The model is consistently too ‘neutron-bright’ in the polar regions and consistently too ‘neutron-dim’ near the equator, with a component that oscillates in value with longitude.

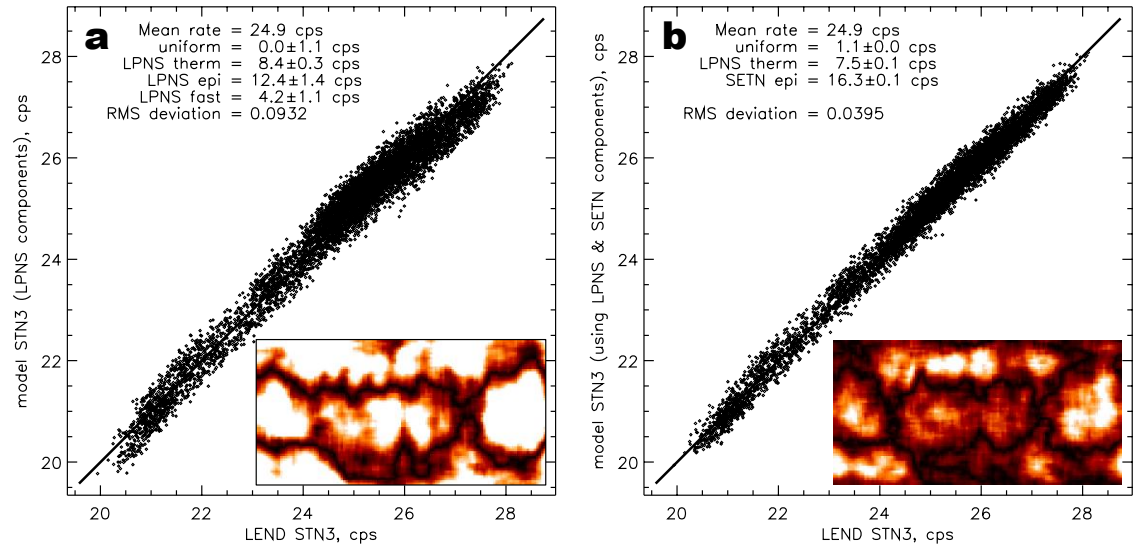

Figure 2: Pixel-to-pixel comparison between data and models for the LEND STN3 detector map constructed from (*a*) a linear combination of LP thermal-, epithermal-, and fast-neutron maps; and (*b*) a linear combination of the LP thermal-neutron map with the map of the LEND SETN epithermal-neutron detector (Fig. 1b). The inset image in each panel is a map of residuals of the fit (absolute value), smoothed to show regional discrepancies, stretched between zero and 1% of the signal maximum.

The LEND epithermal neutron detector SETN offers an alternative model for the epithermal component of the neutron populations detected by the thermal-neutron detector, STN3. Since the SETN detector is identical to STN3, apart from the cadmium foil, it should measure the epithermal and fast-neutron flux that also is intercepted by STN3 and collects measurements simultaneously with STN3, minimizing any systematic effect due to collecting data in different epochs. We can construct a second model for the STN3 map, using the thermal-neutron template from LP and using the map of SETN signal to represent all suprathermal neutrons in a combined LP+LEND model with only three adjustable parameters: lunar thermal neutrons, spacecraft-sourced background, and lunar epithermal (and fast) neutrons.

The variance between model and data is dramatically reduced by using SETN to model the contribution of epithermal neutrons to STN3, as reported in Table 2. There is some flexibility in how to formulate the model. The uncertainty on the uniform component in the LP-based model for STN3 (Table 1) is substantial enough to encompass the background count-rate of 1.04 cps estimated by Litvak *et al.* (2012a), who also estimated a background count rate of 0.72 cps in the SETN detector. These background values included a scale factor of 0.93 to account for changes in neutron moderation and scattering by fuel in the spacecraft, but more recent Monte Carlo modeling of neutron transport in the spacecraft

suggests that moderation by the hydrazine fuel actually has little effect on the population of neutrons generated in the spacecraft that reach the detectors. Reversing this scaling, we thus assume that background in the STN3 and SETN detectors could better be represented by 1.12 cps in STN3 and by 0.77 cps in SETN. The model displayed in Fig. 2b employs a template with the background count rate of 0.77 cps subtracted from SETN prior to normalization, and assumes a fixed value of 1.12 cps for the background count rate in STN3. The result is a clearly superior fit compared to Fig. 2a and the LP-only model: the magnitude of dispersion about the correlation axis is reduced, the dispersion is symmetric about the axis, the map of residual discrepancies between model and data is substantially reduced in magnitude, and the quantitative variance is reduced from 0.0932 cps^2 to 0.0395 cps^2. An alternative is to fit the uniform component as a free parameter, where a negative value for the uniform component in STN3 translates to an estimate for the background count rate that must be subtracted from SETN. This approach yields a slightly better fit to the map of STN3 signal and estimates a background count rate for SETN of 1.3±0.6 cps, about 1σ greater than the SETN background estimated by Litvak *et al.* (2012a). The background count rates in STN3 and SETN prove to be covariant in fitting the two maps jointly, thus the uncertainties are sufficiently generous that there is no compelling statistical argument to prefer the fitted values over the estimates by Litvak *et al*. (2012a) for STN3 and SETN. Using fixed values for the background count rate substantially reduces the precision uncertainties in the remaining parameters. These are the values reported in Table 2.

The variance in the LP+LEND model is reduced from the LP-only model by a factor of 2.4. Testing the ratio of variances, *F*, confirms that this is a superior model with essentially 100% confidence. The background count rate due to spacecraft-sourced neutrons that is assumed from Litvak *et al.* (2012a), 1.12 cps, accounts for a modest 4.5% of total signal, with 65.2±0.5% (16.26±0.12 cps) of the globally averaged STN3 signal in the combined epithermal and fast neutron flux measured by SETN. The component due to thermal neutrons is 30.3±0.4% (7.54±0.11 cps) of all neutrons detected by STN3. Uncertainties in the fit are small since the model has only two free parameters after fixing the background. Since SETN and STN3 data are acquired simultaneously, the fit coefficients enable the flux of thermal neutrons to be determined from the STN3 data by subtracting the background count rate and 1.651 times the SETN detector signal minus its own background:

$$\text{Thermal} = \text{STN3} - 1.651 \bullet (\text{SETN} - 0.77) - 1.12, \quad (1)$$

in which STN3 and SETN represent the signal from those detectors in units of counts per second and the coefficient of 1.651 times the mean signal in SETN (minus background) results in the mean contribution in counts per second from epithermal neutrons detected by STN3. Since data reported from the DLD files correspond to one-second integrations, these coefficients can be applied directly to the data. Data-reduction coefficients estimated

similarly for each of the LEND detectors are summarized in Table 3 with estimated uncertainties.

Analysis of LEND SETN detector: Best-fit coefficients for modeling SETN using LP maps are reported in Table 1, and the correlation between model and data is displayed in Fig. 3a. The dispersion in pixel values about the line of correlation is relatively broad and the axis of the cloud of values is perceptibly tilted such that model values tend to be a little too high when data values are low, and model values tend to be a little too low when data values are high. The systematic discrepancies in the map of residuals between model and data shown in Fig. 3a are similar to the discrepancy seen in modeling STN3 using only LP neutron flux maps, where the model is consistently neutron-bright at high latitudes, and neutron-dim at equatorial latitudes, compared to the SETN map. The coefficient for the uniform component of neutrons detected by SETN is slightly greater than zero at 0.4±0.9 cps (4±8%) of the mean total count rate of 10.622±0.002 cps, well within uncertainty of either zero or the background count rate of 0.77 cps estimated by Litvak *et al.* (2012a). Lunar thermal neutrons contribute a small fraction of the total counts in SETN with 0.3±0.1 cps (3±1%). The epithermal neutron component, 8.0±0.8 cps, accounts for 75±8% of SETN signal. As with STN3, there is a component of fast neutrons detected in excess of the nominal epithermal neutron component, 1.9±0.5 cps, accounting for 18±5% of SETN signal. The total count rate due to suprathermal neutrons estimated from fitting the SETN epithermal detection map using LP map templates is 9.9±0.9 cps, 93±8% of the detected count rate.

As with modeling STN3, a model can be constructed for SETN that is partially based on other LEND data to determine coefficients for subtracting from the SETN signal the background and thermal neutron components of the total, leaving only the combined epithermal and fast neutron detection rate (Fig. 3b). The template for thermal neutron flux is constructed by subtracting the background and SETN contributions from the STN3 map using Eqn. 1, and the background count rate in SETN is assumed to be 0.77 cps as estimated by Litvak *et al.* (2012a), accounting for 7% of the SETN signal. Fixing the background count rate to the calibrated value leaves three free parameters: the thermal-neutron contribution, the epithermal-neutron contribution, and the fast-neutron contribution. The numerical coefficients for this model are tabulated in Table 2. None of the retrieved coefficients are altered beyond the bounds of uncertainty from Table 1, which is not surprising since only minority components are altered from the LP-only fit. Nevertheless, the variance of the best-fit model is reduced to an extent that is a marginally significant improvement over the LP-only model of Fig. 3a and Table 1, a bit better than the 1σ confidence level. In this model, thermal neutrons account for 3±1% of detected lunar neutrons, epithermal neutrons account for 72±5% of detected lunar neutrons, and fast neutrons account for 18±4% of detected lunar neutrons. The total detection rate for suprathermal neutrons, globally averaged, is 9.50±0.13 cps, 89.5±1.2% of the global

643 average signal. The slight decrease in lunar neutron contribution balances the slight
644 increase in the assumed background value.

645

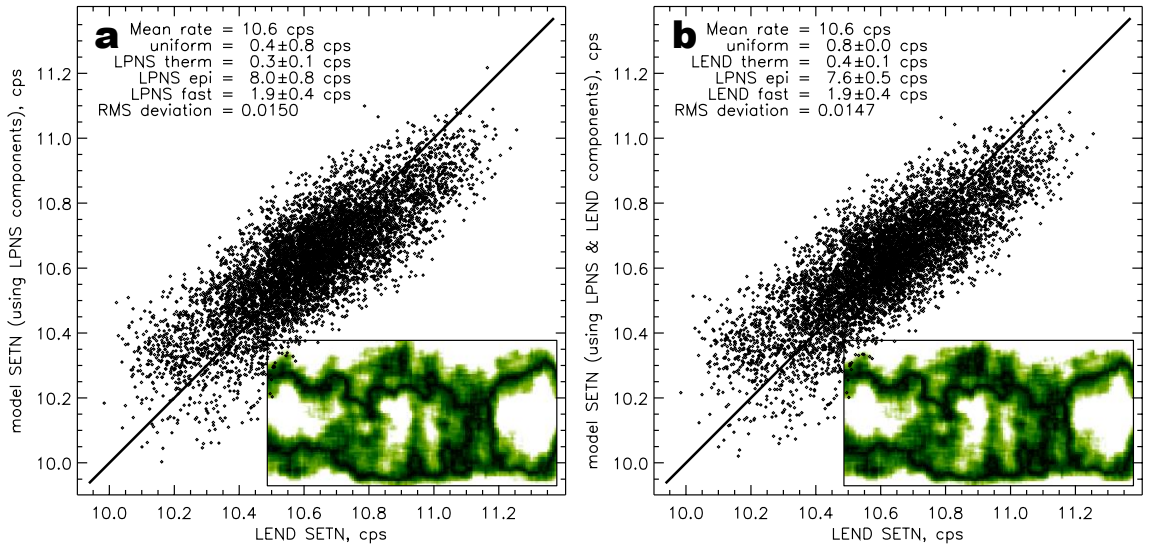

Figure 3: Pixel-to-pixel comparison between data and models for the LEND SETN detector map constructed from (*a*) a linear combination of LP thermal-, epithermal-, and fast-neutron maps; and (*b*) a linear combination of the LP epithermal- and fast-neutron maps with the map of thermal neutron flux evaluated from LEND STN3. The inset image in each panel is a map of residuals of the fit (absolute value), smoothed to show regional discrepancies, stretched between zero and 1% of the signal maximum.

646

647 If the background (spacecraft-sourced) count rates in SETN and STN3 are allowed to be
648 fitted parameters, then the fit to STN3 is improved, but the fit to SETN is degraded such
649 that it is identical to fitting with the LP templates alone. A joint goodness-of-fit criterion
650 for simultaneously estimating the best-fit background to both STN3 and SETN results in
651 such loose constraints that it is no improvement over assuming the calibrated background
652 count-rate values from Litvak *et al.* (2012a).

653 The suprathermal neutron flux can be derived from the SETN signal by subtracting the
654 small spacecraft-sourced background and the small contribution from thermal neutrons:

655 $$\text{Epithermal} = \text{SETN} - 0.047 \bullet \text{Thermal} - 0.77, \qquad (2)$$

656 in which the coefficient of 0.047 applied to the thermal neutron flux results from dividing
657 the mean thermal neutron flux computed from Eqn. 1 into the mean contribution in counts
658 per second from the fit parameters. The result of Eqn. 1 can be substituted for the Thermal
659 component and terms combined to yield:

660 Epithermal = 1.0776•SETN – 0.047 • STN3 – 0.777, (3)

661 in which STN3 and SETN represent the signal from those detectors in units of counts per
662 second. Table 3 summarizes the coefficients in these expressions, with estimated
663 uncertainty. The small numerical increase in the overall SETN count rate in the first term
664 counters the subtraction of lunar epithermal neutrons that are detected by STN3 in the
665 second term.

666

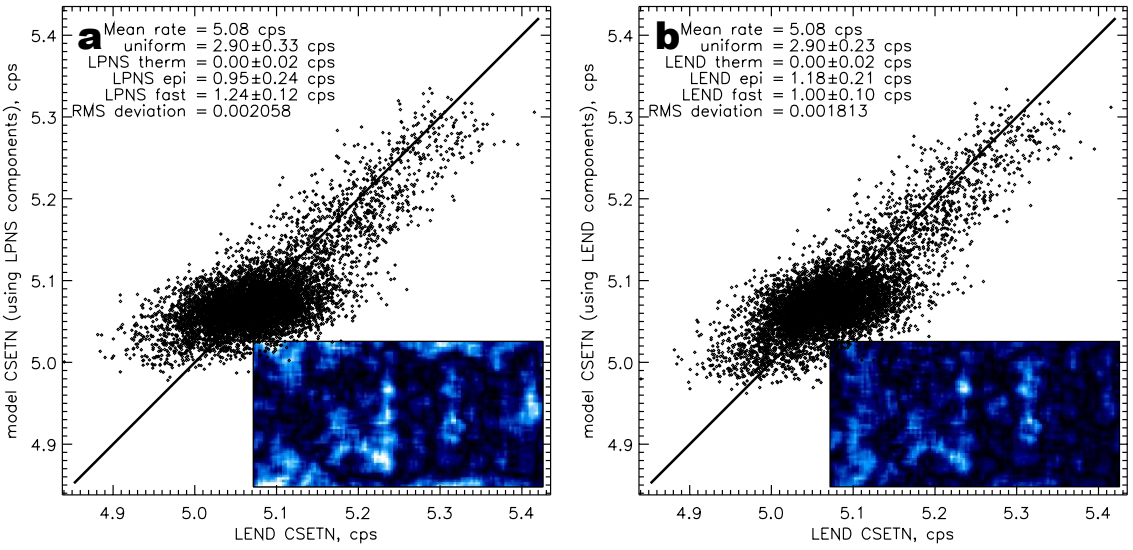

Figure 4: Pixel-to-pixel comparison between data and models for the LEND CSETN detector map constructed from (*a*) a linear combination of LP thermal-, epithermal-, and fast-neutron maps; and (*b*) a linear combination of the LP fast-neutron map with the maps of thermal and epithermal neutrons estimated from the LEND STN3 and SETN detectors respectively. The inset image in each panel is a map of residuals of the fit (absolute value), smoothed to show regional discrepancies, stretched between zero and 1% of the signal maximum. Both models yield zero sensitivity to thermal neutrons and nearly the same uniform background from spacecraft-sourced neutrons.

667

668 *Analysis of LEND CSETN detector*: Combining total counts across the operating CSETN
669 detectors, divided by total integration time across all operating detectors, yields the average
670 count rate per pixel per detector. Multiplication by four yields the equivalent of total
671 CSETN count rate as if all four detectors were operating at all times, for a geographic
672 average of 5.082±0.001 cps. The instrument anomaly in May 2011 reduced CSETN to two
673 operating detectors (CSETN3 and CSETN4) and it has continued to collect data in that
674 mode. Small differences in background levels and the sensitivity specific to each detector
675 are corrected by scaling each individual detector's signal and its background to yield the

676 average value of signal above background averaged over all four detectors, so that
677 discontinuities are not introduced by changes in the identity of which CSETN detectors are
678 in operation. The analysis of the individual CSETN detectors is presented later, after
679 covering the combined CSETN detector system to demonstrate the methodology.

680 Best-fit coefficients for modeling CSETN using LP maps are reported in Table 1, and the
681 correlation between model and data is displayed in Fig. 4a. CSETN pixel values cluster
682 into two groups, a minority formed by highly-correlated bright pixels in the model and data
683 that follow the correlation axis, and a majority of pixels that cluster at low data values,
684 consistent with the extensive neutron-dim regions shown in the map of Fig. 1c. There do
685 not appear to be major regional discrepancies between model and data. The estimated
686 uniform background component is a much greater fraction of total signal than in the SETN
687 detector, accounting for 2.9±0.3 cps or 57±6% of the total. This value is greater than the
688 total background level of 2.42 cps estimated by Litvak *et al.* (2012a) by more than 1σ; we
689 thus continue to use the background detection rate as a fitted parameter.

690 The SETN and CSETN detectors differ only in that the four CSETN detectors are located
691 inside the collimator structure. The average background per detector in CSETN is
692 0.72±0.08 cps, very similar to what we estimate for SETN. The high relative background
693 in CSETN thus is due to the collimator reducing the reception of lunar signal while largely
694 preserving the rate of spacecraft-sourced neutron detections. The similarity between SETN
695 and CSETN background count rates, despite the isolation of the CSETN detectors inside
696 the collimator, suggests that the primary source of detected epithermal neutrons is material
697 in close proximity to the detectors. The thermal-neutron contribution to CSETN is zero,
698 with narrow uncertainty. Lunar-sourced suprathermal neutrons account for the remaining
699 globally-averaged count rate of 2.2±0.3 cps or 43±6% of total CSETN counts, combining
700 neutrons both in and out of collimation, both fast and epithermal populations. The fast-
701 neutron contribution to the total CSETN signal, 1.24±0.12 cps, is a greater fraction of the
702 total than in the other LEND detectors, 24±2% of total count rate or 57% of lunar-sourced
703 neutrons. Epithermal neutrons, comparable to the population detected by LP, account for
704 0.95±0.24 cps; 19±5% of the total count rate or 43% of lunar-sourced neutrons. The net
705 population of suprathermal neutrons detected by CSETN is skewed towards higher
706 energies, as expected.

707 The thermal and epithermal neutron maps derived from STN3 and SETN using Eqns. 1
708 and 2 can be substituted for the corresponding LP maps as templates for modeling CSETN.
709 Since SETN and CSETN use identical detectors, they should have approximately the same
710 response to the lunar neutron energy spectrum that propagates through free space before
711 reaching the detector. Fig. 4b shows the comparison between model and data pixels using
712 these substitutions, with numerical coefficients of the fit tabulated in Table 2. The change
713 in the comparison between model and data is relatively minor to the eye, but the numerical
714 improvement in the variance is definite and the uncertainty in the fitted parameters is

reduced. The uniform background component and thermal-neutron components are unchanged within uncertainty limits; 57±4% of CSETN signal is in spacecraft-sourced background (2.90±0.23 cps), with no sensitivity to lunar thermal-neutron flux. The relative contributions from epithermal and fast-neutron components are reversed, with 1.18±0.21 cps arising from a map similar to the SETN epithermal neutron map, and 1.00±0.10 cps arising from fast neutrons. Since there is no thermal-neutron contribution, the HEE neutron flux detected by CSETN is obtained simply by subtracting the uniform background component:

$$\mathrm{HEE} = \mathrm{CSETN} - 2.90, \quad (4)$$

in which CSETN represents signal from the CSETN detector in units of counts per second, and HEE represents the total lunar neutron flux measured by CSETN, including neutrons that reach the detectors in collimation as well as those neutrons that reach the detectors through the wall of the collimator. Table 3 includes the estimated background used in Eqn. 4.

The spacecraft-sourced background count rate estimated for CSETN is greater than the estimate of 2.42 cps (48%) by Litvak *et al.* (2012a), and is slightly greater than the estimate of 54% by Eke *et al.* (2012). The background reported in Eqn. 4 and Table 2 is 2σ greater than the published Litvak *et al.* estimate, translating to 97.5% confidence that the background actually has some value greater than 2.42 cps. The estimate by Litvak *et al.* (2012a) for background count rates at the Moon included an assumed 7% decrease in spacecraft-sourced neutron background due to fuel consumption that is probably incorrect according to more recent work by Litvak *et al.* (2016). Compensating for this erroneous correction brings the background of Litvak *et al.* (2012a) up to 2.60 cps, while the more recent work by Litvak *et al.* (2016) estimates 2.74±0.09 cps, similar to the value from Eke *et al.* (2012). For internal consistency, we stand by the value we have derived from the operational data, since no single one of the determinations by Litvak *et al.* (2016), Eke *et al.* (2012) or ourselves is clearly preferable to another. The distinction is less than one uncertainty unit using our estimate for uncertainty, less than 2σ using the estimate from Litvak *et al.* (2016).

Estimates for collimated component of CSETN detected signal: We consider the SETN-like contribution to the CSETN signal to be an upper limit on the total signal from neutrons that reach the detectors in collimation, 1.2±0.2 cps or 54±11% of lunar neutrons, since the SETN template includes both the epithermal and fast components of the neutron energy spectrum as it is encountered by a detector in the open but adjacent to the LEND collimator. Neutrons in the thermal and epithermal range that are out of collimation are moderated and stopped, skewing the out-of-collimation spectrum towards neutrons of greater initial energy at the point of emission, represented by the fast neutron component in the fit to the CSETN map. If any fraction of epithermal neutrons were also to penetrate the collimator,

753 it would reduce the fraction assigned to detection in collimation, consistent with 1.2 cps
754 being an upper limit. Only if the in-collimation fraction of neutrons detected by CSETN
755 were richer in fast neutrons than the spectrum detected by SETN could this be an
756 underestimate. Since much of the dispute over the effectiveness of a collimated detector
757 has been based on claims of very low collimation efficiency (Lawrence *et al.* 2010;
758 Teodoro *et al.* 2014), the possibility that 1.2 cps is an underestimate of the collimated
759 counting rate is not a significant issue. A serviceable working estimate for neutrons
760 received in collimation would be the epithermal detection rate estimated from modeling
761 with LP templates, 1.0±0.2 cps in collimation, or 45% of lunar neutrons detected in
762 collimation.

763 An alternative estimate for the fraction of epithermal neutrons received in collimation
764 comes from the empirical angular sensitivity function presented for CSETN by Litvak *et*
765 *al.* (2012a), which has a high-throughput core for an opening angle from nadir to about 12°
766 from nadir, where the measured neutron transmission is near zero. Neutron transmittance
767 increases from this minimum in a wing that extends out to 90° from nadir, although the
768 limb of the Moon only extends to 76.4° from nadir at the 51 km altitude of LRO. The
769 integrated signal within the core region is about 50% of total signal integrated over the
770 angular sensitivity function, including a cosine anisotropy for emission from the surface
771 and limiting the numerical integration to 76.4° from nadir. Applying this 50% fraction to
772 the entire HEE population detected by CSETN yields 1.1 cps. A lower limit can be
773 estimated by assuming that detected fast neutrons always are out of collimation and apply
774 this modulation factor to the SETN-like fraction only. This suggests a lower limit at 50%
775 of 1.2±0.2 cps, or 0.6 cps.

776 Lawrence *et al.* (2010) predicted the count rate for a collimated neutron detector by
777 comparison to the LP uncollimated epithermal neutron detector, arriving at a very low
778 value for a detector resembling LEND CSETN in design. This calculation incorporated
779 several assumed parameter values that are not needed in a comparison between LEND's
780 uncollimated and collimated detectors, including GCR flux and spectrum and proportional
781 counter efficiency. Equation 20 of Lawrence *et al.* (2010) estimates that the field of view
782 of a single collimated detector is 0.0109 of the FOV for an uncollimated detector at the
783 LRO altitude. The count rate for lunar epithermal and fast neutrons detected by SETN is
784 9.5–9.9 cps (Tables 1 & 2). The predicted detection rate by all four CSETN detectors for
785 lunar neutrons in collimation is thus 4•0.0109•9.5 cps = 0.41 cps by this calculation, a
786 factor of 2.8 greater than the estimate by Lawrence *et al.* (2010). A Monte Carlo calculation
787 for the collimator performance, whose details are not shown by Lawrence *et al.*, increases
788 the count rate by 20%. Applying this same correction, we estimate 0.49 cps in collimation.
789 Lawrence *et al.* also argue that neutrons propagating along the length of the detectors in
790 CSETN experience partial shielding from the active volume of the detector by ^{3}He in a
791 "dead zone" at the end of the detector, reducing the detectable neutron flux to ~0.76 of

nominal, bringing the count rate in collimation to 0.37 cps. It is not clear whether this correction factor applies, since the increase in detector sensitivity after switch-on that is reported by Litvak *et al.* (2012a) appears to result from the "dead zone" becoming active. The collimated component of the neutron flux detected by CSETN then falls within the range 0.37–1.2 cps out of a total of 2.2 cps for HEE neutrons, with 17% – 54% of lunar HEE neutrons detected by CSETN in collimation, or 7% to 24% of all neutrons detected by CSETN, including the spacecraft-sourced background.

Lawrence *et al.* (2010) make the simplifying assumption of isotropic neutron emission from the Moon, which is unrealistic and presents significant consequences. The actual condition of anisotropic emission decreases the broad FOV of uncollimated detectors, which extends out to the lunar limb. The surface emission angle is 90° from local zenith at the horizon, with zero emission. The empirically-determined 45 km FWHM field of view for the LP neutron detectors extended to about 37° from nadir, much less than the 79° from nadir to limb at 30 km altitude. As a test for the effect of anisotropy, the solid angle contributing to the SETN detection can be reduced by the mean of the cosine function from 0° to 90°, which is 0.637, approximating the reduction in field of view due to cosine emission anisotropy. This reduced solid angle corresponds to an angle from nadir of 59.1° (~83 km radius on surface). Applying this angle in the preceding calculations yields an estimated count rate in collimation of 1.2 cps, or 0.9 cps with the assumption of self-shielding. Predictions from this model for a collimated detector thus are dominated by the quality of assumptions that are difficult to constrain.

Teodoro *et al.* (2014) provide an additional test on performance of the CSETN detector system's angular sensitivity and the fraction of signal received in collimation versus flux detected out of collimation. They test performance of two hypothetical systems, one with zero sensitivity to neutron flux in collimation, and one with significantly greater sensitivity in collimation as well as reduced background compared to the results here, based on an early characterization of the detector performance by Mitrofanov *et al.* (2011). Between these two cases, Teodoro *et al.* (2014) favor a condition with greater background and near-zero signal in collimation. They did not derive an optimal description of CSETN performance, so it is not clear how to compare their result to the intermediate description of spacecraft background and collimated signal derived here and by Litvak *et al.* (2016) in independent analysis.

Analysis of individual CSETN detectors: The four detectors comprising CSETN are reported by Litvak *et al.* (2012a) to have slightly different background count rates, and may be expected to have slightly different sensitivity. The four detectors can be mapped individually and fitted individually. Since the combined CSETN detectors are best fit using thermal and epithermal neutron maps derived from STN3 and SETN plus the LP fast-neutron map, we model the individual CSETN detectors using these components and report the fit coefficients in Table 4 to obtain the components of spacecraft- and lunar-sourced

neutrons. The ratio between epithermal and fast-neutron components for each detector differs from the combined CSETN detector but lies within the uncertainty of the retrievals. The sum of the estimated backgrounds is 2.96±0.21 cps, slightly different from the background estimated for the combined measurement but well within uncertainty. Similarly, the sum in each parameter over all four detectors is within uncertainty of the corresponding parameter fitted to the combined CSETN map, with similar combined uncertainty.

If all four CSETN detectors were in operation at all times, the summed parameters should be identical with the results from fitting the map of the combined signal, but that is not the case. To prevent discontinuities in the CSETN data set due to the changing identity of the operating detectors, the signal and estimated background in each detector is normalized to the geographical average value of lunar HEE neutron count rate per detector, dividing by the geographically averaged count rate in each individual detector:

$$S_x = (\Sigma_n (CSETN_n - BKD_n)/4) / (CSETN_x - BKD_x) \quad (5)$$

where the signal value $CSETN_x$ and the background value BKD_x correspond to the geographical average for each individual detector designated by the subscript x. Multiplying the measured counts and estimated background counts in each detector by its scale factor S_x, each detector obtains the same geographically-averaged net signal. After multiplying by the scale factor S_x, the net counts summed over all operating CSETN detectors, divided by the net integration time over all operating detectors, yields a map of the average count rate per detector. The scaling factors are reported in Table 4. The sensitivity of each individual CSETN detector is within 15% of the mean sensitivity to lunar neutrons.

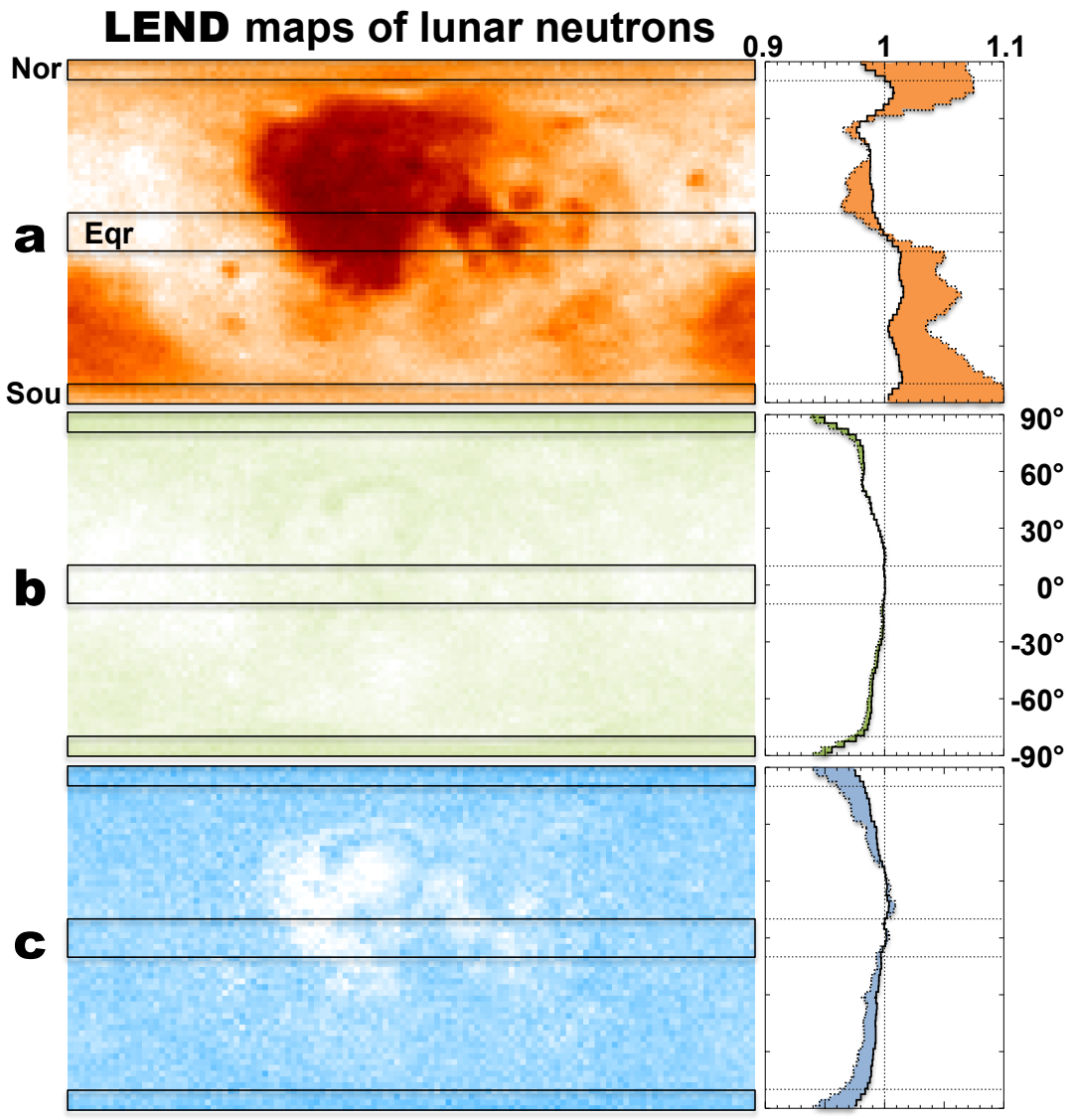

Figure 5: Thermal, epithermal, and HEE neutron maps (*a*, *b*, *c*, respectively), derived from LEND STN3, SETN, and CSETN detectors respectively by subtracting background and out-of-band contributions, stretched from zero to maximum signal to show image contrast. Greatest contrast is in the thermal map (*a*), where neutron flux in the nearside Maria and farside Aitken Basin regions is much less than in the northern hemisphere far-side highlands. Least contrast is in the epithermal map (*b*) where highlands are slightly brighter, while the poles, Maria, and Aitken Basin are slightly darker, but otherwise the map contrast is very small. HEE (*c*) is brightest in the Maria and major nearside craters, bland elsewhere. Black boxes within 10° latitude of the poles and within ±10° of the equator show regions over which signal is averaged to evaluate equator-to-pole signal contrast. Profiles on the right show zonal-average equator-to-pole profiles in the raw data (solid) and in the background-subtracted data (dotted), shading the separation between them.

855

Polar Hydrogen

The motivation for neutron remote sensing on LRO is to investigate the accumulation of hydrogen in the Moon's polar regions. Figure 5 illustrates the contrast in neutron flux between equator and pole and across the map, with background and out-of-band contributions subtracted from each detector according to the coefficients of Table 3 to yield maps of thermal, epithermal, and HEE neutron flux. Regions selected for an equator-to-pole comparison are shown within 10° latitude of the North and South poles and within ±10° of the equator.

Regolith geochemistry strongly influences the thermal neutron flux, so it is not straightforward to interpret hydrogen content from the pole-to-equator contrast in this energy range. For the epithermal and HEE neutron populations derived from SETN and CSETN, the pole-to-equator contrast is related to the regionally averaged abundance of hydrogen trapped in the polar regolith compared to the relatively volatile-free equatorial regolith, with a lesser effect from regolith composition on neutrons in this energy range. The equatorial region features the greatest zonal average epithermal and HEE flux, consistent with the least resident hydrogen, as expected for the latitude that also experiences peak diurnal surface temperature (Vasavada *et al.* 2012). Recent work has demonstrated diurnally varying neutron suppression at the equator that is ignored here (Livengood *et al.* 2015), since the present work constructs maps from measurements at all local times, diluting the small diurnally varying suppression. We use the zonal-average and diurnal-average neutron flux near the equator as the reference for dry regolith everywhere on the Moon, including both the maria and highlands regions in the average.

Each of the maps displayed in Fig. 5 is accompanied by a meridional trace of the zonal-average signal as a function of latitude. The thermal neutron signal is highly variable with latitude, with a maximum at the poles ~9% greater than the equatorial average signal. The epithermal neutron flux measured by SETN declines gradually up to about 75° latitude, then declines sharply to ~94% of the equatorial signal at the poles. The modest background and thermal neutron signal subtracted from SETN to reveal the epithermal neutron signal makes little difference in the meridional trace from equator to pole. The much more significant spacecraft-sourced background subtracted from CSETN results in a meridional trace for HEE flux that differs in detail from the epithermal distribution but reaches the same signal suppression at the poles. The similarity in pole-to-equator contrast of the epithermal and HEE distributions cannot be an artifact of using the LEND epithermal map in modeling CSETN to obtain the spacecraft-sourced background, since both the LP-based and LEND-based models for CSETN obtained the identical background estimate. The only quantity subtracted from the CSETN data to form the map and trace in Fig. 5 is the uniform background.

Neutron flux measurements extracted from near the poles and the equator are tabulated in

Table 5 for the LP neutron data products, for the LEND detectors, and for the thermal, epithermal, and HEE neutron count rates derived from the LEND detectors. The precision uncertainty in the detector signal is estimated using standard error of the mean for the population of measured map pixels in each comparison region, for both LP and LEND. The uncertainty tabulated for the background-subtracted LEND measurements is the accuracy uncertainty estimated from the tabulated fit parameters in Tables 1 to 3, since the precision uncertainty is much smaller than the accuracy uncertainty for the subtracted background and out-of-band contributions. The accuracy uncertainty is not independent in equator-to-pole comparisons: it applies equally to both regions, in the sense that if the background is a little over-estimated at the pole, it is overestimated to the same extent at the equator. The accuracy uncertainty in the ratio between equator and polar signal is estimated by constructing a normal distribution of discrepancy values with the appropriate standard deviation and adding values from this population equally to both numerator and denominator to create a randomly-distributed population of ratio values whose mean and standard deviation can be computed to yield the accuracy uncertainty in the ratio. This is the approach used in Tables 5 and 6.

The raw LEND STN3 signal is about the same at the poles as at the equator. After subtracting the background and epithermal components, the thermal neutron flux measured by LEND within 10° of the north pole is 6.8±0.1% greater than the equatorial flux, and the thermal neutron flux measured at the south pole is 10.9±0.1% greater than the equatorial flux. The equivalent ratios for LP neutron flux measurements are 10.8±0.2% greater at the north pole and 14.8±0.2% greater at the south pole. Greater polar flux in the LP measurements is consistent with the residuals from modeling STN3 using LP maps.

Signal suppression measured in the raw SETN signal and in the epithermal neutron flux derived from it is about the same, suppressing the signal relative to equatorial by 4.4–5% in the north and by 3.7–4.4% in the south. Suppression in the LP epithermal flux is much less, only 1.6% and 1.8%, respectively, but the suppression in the LP fast-neutron flux is similar to the LEND epithermal contrast, 4.3% and 4.0%, at north and south respectively. Greater polar flux in the LP epithermal neutron flux data is consistent with the residuals from modeling SETN using LP neutron emission maps.

Measured neutron flux suppression can be converted to estimated hydrogen content in the regolith with an appropriate calibration function. Mitrofanov *et al.* (2010a) display calibration curves derived from Monte Carlo calculations for the neutron flux suppression expected with regolith that is evenly implanted with hydrogen, which is summarized as 4.5% suppression corresponding to 100 ppmw hydrogen. The suppression curve can be approximated well by an expression that is inversely proportional to the concentration of hydrogen for large concentrations and approaches unity (no suppression) for very small concentrations:

$$C_1/C_0 = 1 / (1 + [H]/\Gamma_H), \quad (7)$$

where C_0 is the reference count rate from non-hydrated regolith, C_1 is the count rate over hydrated regolith, [H] is the concentration of hydrogen in the hydrated regolith, and Γ_H is a calibration constant in units of hydrogen concentration by weight. This expression can be inverted to yield the estimated hydrogen concentration corresponding to measured count rates,

$$[H] = \Gamma_H \bullet (C_0/C_1 - 1). \quad (8)$$

With 4.5% suppression, the ratio C_1/C_0 will have the value 0.955. With corresponding 100 ppmw hydrogen concentration, the calibration constant Γ_H has a value of 2122 ppmw. Since the mass of a water molecule is 9 times the mass of its hydrogen, the units of the constant can be converted to yield a calibration constant for the weight-percentage of water-equivalent hydrogen (WEH), Γ_W = 1.91 wt% WEH. Calibrations by Feldman *et al.* (1998b) and by Lawrence *et al.* (2006) differ in detail but produce similar results for flux suppression of several percent. Calibration factors from Feldman *et al.* (1998b) suggest that fast neutrons are about five times less sensitive than epithermal neutrons, thus a similar degree of flux suppression in fast neutrons would indicate about five times greater hydrogen content in the observed regolith. A detailed Monte Carlo calculation to calibrate response in the HEE neutron population contributing to CSETN clearly is necessary.

Although the calibration expression is formulated with respect to a reference count rate of C_0 from a nominally hydrogen-free sample of regolith, the reality is that there is always a small amount of hydrogen or water present in most surfaces and thus even the driest and most hydrogen-free reference region on the Moon is not completely devoid of hydrogen. At the small concentrations relevant to lunar materials and the resulting modest neutron flux suppression, the comparison between a minimally hydrated reference region and a more-hydrated region of interest results in a differential value of hydrogen concentration. For example, if a reference sample of regolith were relatively highly hydrated, at [H] = 50 ppmw (0.045 wt% WEH), and a target sample yielded a count rate with 5% flux suppression relative to the reference sample, then the ratio between the count rates would suggest the target has [H] = 112 ppmw (0.1 wt% WEH), whereas the actual hydration of the target sample would be [H] = 164 ppmw (0.148 wt% WEH), very close to the sum of the differential and the reference hydration values. The greater the concentration of hydrogen in the reference sample, the less closely the relative suppression resembles a simple differential measurement in the hydration quantities.

Table 5 applies the calibration expression equally to both LEND and LP epithermal neutron suppression at the pole relative to the equator so that they can be compared with similar terms. The average regolith water content within 10° of the north pole determined from the LEND epithermal neutron flux measured by SETN is 0.100±0.001 wt% WEH by this calibration, and 0.089±0.001 wt% WEH within 10° of the south pole. These values use the

uncertainty in accuracy due to the uncertainty in the background value; the contribution from the precision uncertainty is negligible. The average concentration from the LP epithermal data, using the same calibration, is 0.031–0.035 wt% WEH with similar narrow uncertainty. A lower limit can be estimated from the SETN count values with no background subtraction, 0.087 wt% WEH at the north pole, and 0.074 wt% WEH at the south pole. The discrepancy between LEND SETN and LP epithermal is well beyond measurement uncertainty, which we address below. Note that the differential in hydrogen abundance between poles and equator from the contrast in neutron flux measured by SETN is comparable to the example just given for the differential effect in measuring two samples with different quantities of hydrogen included. The example included a relatively high concentration in the reference sample, but the actual concentration of hydrogen in equatorial regolith is expected to be much less than in the polar regions.

For CSETN, the estimated uncertainty in the HEE flux is just the uncertainty of the uniform background component. The north polar HEE neutron flux is suppressed by 5.1±0.6% relative to the equator, while the south polar flux is suppressed by 4.8±0.5%. The polar suppression in the LEND HEE flux is similar to the polar suppression in the LEND epithermal flux. Applying the calibration to the HEE suppression yields about the same water-equivalent hydrogen content as the epithermal flux suppression, (0.09-0.10)±0.01 wt% WEH at both poles. The calculations that generated the modeled neutron-suppression calibration factor (Eqn. 8) may not accurately apply to the higher-energy end of the epithermal neutron spectrum that contributes about half the measured HEE signal. Neutrons that truly fall into the fast population, with energy greater than about 1 MeV, are not expected to respond significantly to the presence of hydrogen in the regolith and their presence may dilute flux suppression and thus underestimate the quantity of hydrogen. Calculations have not yet been reported explicitly for populations, with energy between ~10 keV and 1 MeV. However, Lawrence *et al.* (2011b) have investigated the effect on the neutron energy spectrum from the burial depth of hydrogen in the regolith. A qualitative reading of their figures indicates that HEE neutrons respond to approximately the same extent as low-energy epithermal (LEE) neutrons to uniformly hydrogenated lunar regolith, but respond more strongly than LEE neutrons if hydrogen is isolated near the surface, within ~20 cm or less. Similar suppression in both the HEE and LEE neutron populations, measured by CSETN and SETN, respectively, suggests a uniform density of hydrogenation in the polar regolith within the ~1 m depth probed by LEE neutrons. If there is a difference in sensitivity between the HEE and LEE neutron populations, the calibration factors of Feldman *et al.* (1998b) suggest that similar flux suppression would imply up to five times greater hydrogen abundance in the upper ~20 cm of regolith.

The thermal and epithermal neutron flux relative to the equator measured by LP in the polar regions is significantly greater than estimated from LEND data, as shown by the systematic high latitude discrepancy in the model results and reported in Table 5. This distinction also

1009 is noted by Eke *et al.* (2012) in the comparison between CSETN and LP epithermal neutron
1010 flux measurements. Suppression in the LP epithermal neutron flux measurements have
1011 been interpreted as the spatially diluted effect of under-resolved deep suppression in a
1012 limited number of isolated permanently shadowed regions (Lawrence *et al.* 2006). We
1013 interpret the mapped flux as indicating a broad regional distribution of hydrated regolith at
1014 high latitude that is punctuated by locally greater concentrations of hydrogen as reported
1015 by Sanin *et al.* (2012). The regional character of the suppression is apparent in Fig. 6, which
1016 combines the LEND maps of thermal, epithermal, and HEE neutron flux into a three-color
1017 image, assigning the low-energy thermal neutron count rate to red, the moderate-energy
1018 epithermal count rate to green, and the high-energy-skewed HEE count rate to blue. The
1019 regional suppression of epithermal and HEE neutrons is obvious at latitudes above 80°,
1020 where the map shows elevated thermal neutron flux and suppressed epithermal neutron
1021 flux over the entire range of longitude, neatly ending at about 80° latitude. The pole is over
1022 the horizon for measurements below 87° north or south latitude, thus the broad regional
1023 suppression at 80°–87° latitude cannot be due to averaging flux suppression near or at the
1024 poles over all longitudes by the broad spatial footprint of the LEND detectors.

1025 The discrepancy between the suppressed polar epithermal neutron flux measured by LEND
1026 and the lesser epithermal-neutron suppression and greater thermal-neutron enhancement in
1027 the broad polar regions mapped by LP can be resolved by positing a modest systematic
1028 error of ~3% in corrections for the geometric projection of the LP proportional-counter
1029 detectors as a function of latitude. The LEND detectors maintain stable orientation relative
1030 to the surface and thus do not require geometric correction, whereas the thermal and
1031 epithermal neutron detectors of LP both required an identical correction. The fractional
1032 difference in signal contrast between LP detectors and LEND is of approximately the same
1033 magnitude in both detectors at both poles. Geometric corrections to the LP fast-neutron
1034 flux measurements apparently were more successful, as the equator-to-pole contrast in the
1035 LP fast-neutron measurements are very similar to the LEND epithermal and HEE neutron
1036 populations. We conclude that the Moon's polar regions host a widespread distribution of
1037 regolith that is hydrated to 0.1 wt% water-equivalent hydrogen, or 105±13 ppmw hydrogen,
1038 averaging over the region within 10° of the poles. Miller *et al.* (2012) obtained a similar
1039 quantity by combining LP epithermal neutron counts with SETN counts to evaluate the
1040 differential between the polar region and 70° to 80° latitude, assuming ~50 ppmw hydrogen
1041 (0.045 wt% WEH) in the reference region.

1042

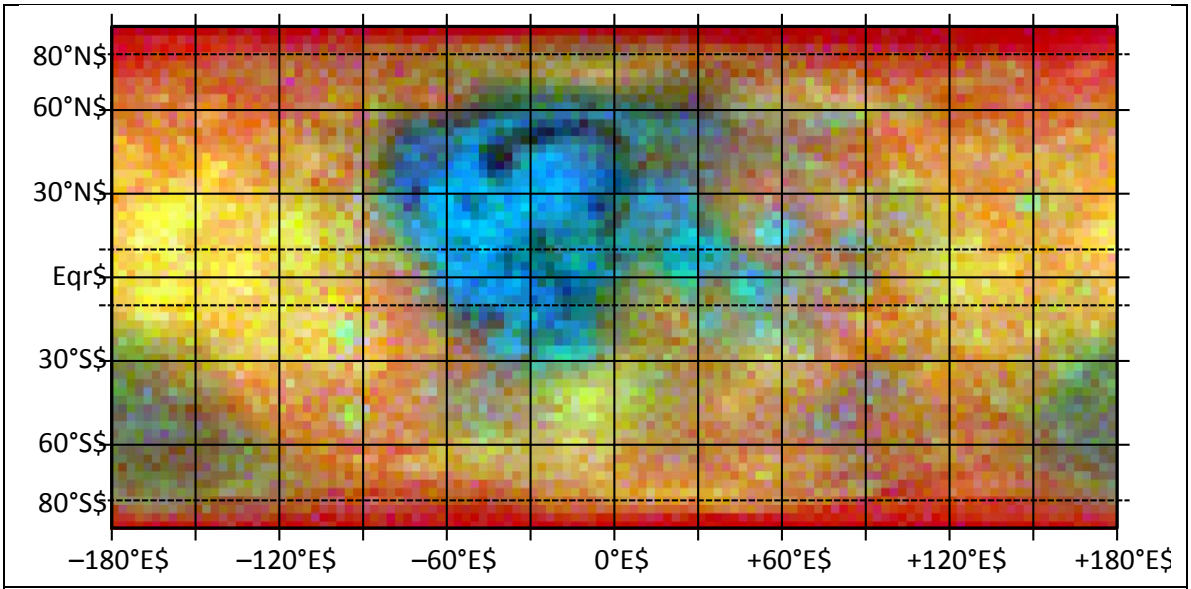

Figure 6: Composite of thermal, epithermal, and HEE neutron flux from LEND. Contrast is stretched between minimum and maximum in each image component. Pole-to-equator comparison regions are shown by dotted lines at 10° latitude difference from the poles and equator. HEE neutron flux (blue), and epithermal neutron flux (green), are suppressed in the polar regions and elevated in the Maria, in the Aitken Basin, and in large craters. The extensive red (thermal-neutron bright) regions at the poles are consistent with broad regional suppression of epithermal neutrons and elevation of thermal neutron flux near the poles.

The meridional profiles for the epithermal and HEE neutrons shown in Fig. 5 decrease monotonically from ~80° latitude to the poles. We consider a second contrast comparison between the region within 2° of the poles and the equator, reported in Table 6. The results are qualitatively similar to the equator-to-pole contrast reported in Table 5 and quantitatively represent a greater concentration of hydrogen in the regolith, 0.12–0.13 wt% WEH with greater than 6σ significance, or 133–144 ppmw hydrogen.

Miller *et al.* (2012) analyze neutron flux measurements differently, by mapping the data in two dimensions rather than the zonal averages used in forming the meridional profiles used here, which sacrifice spatial detail for improved signal-to-noise ratio. Miller *et al.* conclude that suppression in the fast neutron flux measured by LP is significant relative to a reference measurement at 70°–80° latitude only within 2° of the south pole, from which they conclude that Shackleton Crater is unique in having hydrogen near the surface of the regolith and that elsewhere, the upper ~20 cm of regolith is hydrogen-poor. We observe that the meridional profile in the LEND epithermal and HEE neutron count rates, and the LP fast neutron count rate, is suppressed to the same extent relative to the equator at both poles. We conclude that the identification of Shackleton Crater as a distinct locus is not

supported and that it is only by coincidence that Shackleton Crater falls on the maximum in a regional pattern of hydrogen distribution controlled by lunar latitude.

The equatorial zonal average that is used here for the reference neutron flux measurement for epithermal (LEE) and HEE neutron populations may be skewed by the fact that it includes both maria and highlands regions, which differ in the mapped flux measurements (Figs. 1, 5, 6). If the reference region were restricted to just the highlands, it would increase the LEND epithermal reference value by about 0.7%, and decrease the HEE reference value by about 1.5%. The calibration expression can be applied to these relative differences in the reference rates, implying that with a highlands (non-Maria) reference, the WEH hydrogen content derived from the LEND epithermal (SETN) data would increase by 1.91•(100.7/100-1) = 0.013 wt% WEH, while the content derived from the HEE flux would decrease by 1.91•(98.5/100-1) = -0.029 wt% WEH. Applying these differences to the tabulated values in Table 5, the estimated water content averaged over both poles rises from 0.094 wt% to 0.107 wt% estimated from epithermal neutron flux, and decreases from 0.095 wt% to 0.066 wt% estimated from the HEE neutron flux. These values would be consistent with a somewhat dryer upper regolith at the poles in the top ~25 cm compared to the deeper regolith probed by the lower-energy emergent neutron flux. The choice of the reference region should have no effect on comparisons between LP- and LEND-based retrievals of hydrogen content in the polar regions, as the reference is constructed from the measured flux in the same regions.

Hydrogen Outside the Polar Region

It is now known that the Moon features widespread surface hydration that appears to increase with angular separation from the subsolar point (Pieters *et al.* 2009; Sunshine *et al.* 2009; Clark 2009; Hendrix *et al.* 2012), thus increasing with latitude as well as increasing towards the terminator. The variation with respect to the terminator has been interpreted by Sunshine *et al.* (2009) as actual diurnal variability, rather than an optical effect as interpreted by Clark (2009). Sunshine's interpretation is supported by a similar pattern in nadir-viewing ultraviolet spectroscopy from LRO (Hendrix *et al.* 2012), and by LEND measurements of diurnal variability in the epithermal neutron flux near the equator (Livengood *et al.* 2015), which is not subject to effects of viewing angle. If the diurnally varying component of the spectroscopic hydration signature is not an optical effect, then there would be no cause to dismiss the static distribution as a function of latitude as an optical effect, either. This raises the possibility that the distribution of epithermal neutron flux with latitude may be affected by a spatially varying distribution of hydrogen in the lunar regolith.

The zonal average epithermal and HEE neutron flux declines from near the equator to the poles, diminishing more steeply polewards of ±80° latitude (Fig. 5). The epithermal neutron flux is diminished by ~2% at ±80° latitude, corresponding to ~0.04 wt% WEH or

40 ppmw hydrogen if this suppression were entirely assigned to the effect of hydrogen in the regolith. The HEE flux is diminished somewhat more, but quantitative interpretation is complicated by the obvious presence of local brightening associated with the Maria (Figs. 1, 6). Hydration values detected in reflected light have not been well quantified, but values on the order of 0.1 to 0.3 wt% were suggested in the discovery papers. The increase in the surface hydration signature at higher latitudes is qualitatively consistent with the diminishing epithermal neutron flux detected by LEND, if the hydrated layer were not a "monolayer" but extends into the ground by a few centimeters at the concentration interpreted from spectroscopy. Modeling by Lawrence *et al.* (2011b), cited in the discussion of polar volatiles, suggests that hydrogen in shallow emplacement suppresses HEE neutrons to a greater extent than LEE neutrons, qualitatively similar to the observed pattern. A first-order estimate for the depth of hydration at 0.1–0.3 wt% that would yield 0.04 wt% WEH for the one-meter depth probed by SETN (LEE neutrons) is a layer extending from the surface to 13–40 cm depth in the high-latitude region of greatest suppression, at ~80° latitude. A more precise statement on the depth and degree of hydrogenation that could correspond to the observed neutron suppression will require new Monte Carlo calculations for the neutron leakage flux under suitable conditions. Lawrence *et al.* (2011b) found that for a relatively thin near-surface layer of modest hydration, the measurable epithermal neutron flux could actually be enhanced by a few percent. Significant effort will be required to quantitatively interpret the apparent observed condition of weakly suppressed neutron flux in both LEE and HEE neutron populations.

A study by Little *et al.* (2003) suggests that subsurface temperature in the regolith may make a contribution to suppressing epithermal neutron flux with increasing latitude, resulting in an overestimate of hydrogen in the regolith. Most of the work presented by Little *et al.* (2003) is for thermal neutron flux, but they also show figures depicting emergent epithermal neutron flux as being reduced at low temperature compared to high temperature (<400 K), although to a lesser extent than for thermal neutrons. They investigate the variation with latitude of LP thermal neutron flux in the lunar highlands, differing from the zonal average profile of Fig. 5 by excluding the nearside Maria (near 0° longitude) and South Pole-Aitken Basin (~180° longitude) regions, which have strongly suppressed thermal neutron flux. The highlands-only profile that they present shows a general decrease in thermal neutron flux from the equator to the poles, discernible in the mapped thermal neutron data of Figs. 1 and 5 as darkening from equator to pole within the lunar highlands of the northern farside and southern nearside.

The model presented by Little *et al.*, although qualitatively similar to the variation of thermal neutron flux with latitude in the lunar highlands, exhibits substantially less quantitative contrast from equator to pole than the LP thermal neutron data to which they compare it. If the near-polar flux measured by LP were reduced by a few percent further, as we argue here, then the quantitative discrepancy would be even greater. The neutron

energy spectrum modeled by Little *et al.* extends only to 0.1 keV and thus does not include the HEE neutron population sensed by CSETN. Their published spectra show that regardless of effects at low neutron energy (<1 eV) in response to variations in temperature below 400 K, neutrons of greater energy are indifferent to temperature effects. Thus, the temperature effects cited by Little *et al.* cannot even qualitatively suggest an explanation for high-latitude suppression in the HEE neutron flux aside from the effect of hydrogen or broad latitude dependence in the elemental composition of the regolith.

Conclusions

We have constructed maps of the lunar neutron flux measured by thermal (STN3), epithermal (SETN), and collimated epithermal (CSETN) detectors of the Lunar Exploration Neutron Detector (LEND) on the Lunar Reconnaissance Orbiter mission. Linear combinations of similarly-constructed maps from earlier Lunar Prospector (LP) neutron flux measurements can be used to model the LEND maps and thereby estimate the contributions of neutrons to the detected signal in the LEND detectors from different source populations. Hybrid models that combine LP flux maps with LEND maps reduce systematic discrepancies between the LEND detector maps and models, and provide estimates for parameters to reduce data from the detectors to measurements of the thermal, epithermal, and High Energy Epithermal (HEE) neutron flux populations. Spacecraft-sourced background neutron count rates estimated in this work are consistent within uncertainty with rates determined by Litvak *et al.* (2012a) from calibration measurements for the uncollimated thermal and epithermal neutron detectors, leading us to accept background count rates estimated from Litvak *et al.* for the uncollimated detectors. The background estimated for the collimated CSETN detector is significantly greater than that estimated by Litvak *et al.* (2012a). Uncertainty limits on analytical parameters derived within the present work are generous, as this work does not presuppose any knowledge of the statistical properties of LEND detections and incorporates all covariances in fitting data. The resulting uncertainties estimate accuracy rather than precision, and apply equally to all elements of maps derived from LEND data. As a result, even the relatively large uncertainties estimated here in modeling the background in LEND data have a relatively small influence on the geochemical interpretation of LEND results, which depend on the ratio of signal in regions compared.

This work estimates the contribution of lunar neutrons in collimation to the total lunar neutron detection rate in the LEND CSETN collimated detector. We estimate an upper limit of 1.2 cps in collimation with a serviceable working estimate of 1.0 cps. Using the work of Lawrence *et al.* (2010) applied to a comparison between the LEND collimated and uncollimated epithermal neutron detectors, we set a hard lower limit of 0.37 cps in collimation. This is substantially greater than estimated by Lawrence *et al.* (2010), which differed by estimating CSETN performance from LP data. Our estimation is based on identical detectors in and outside of collimation as part of LEND, operated simultaneously,

thus eliminating parameters that were estimated or assumed in a comparison with the Lunar Prospector measurements. The lower limit is an underestimate for the true detection rate in collimation, as the model developed by Lawrence *et al.* (2010) does not include the effects of emission anisotropy at the lunar surface. A modest approximation for the effect of anisotropic emission significantly increases the estimated count rate in collimation, raising it to ~0.9–1.2 cps. We thus find that the count rate in collimation for the LEND CSETN detector is in the range 0.37–1.2 cps, 17–54% of lunar neutrons detected by CSETN, with 1.0 cps or ~45% as a reasonable estimate for the collimated component. The count rate out of collimation is 1.0–1.8 cps, or 46%–83% of detected lunar neutrons. The estimated count rate using the method of Lawrence *et al.* (2010), corrected for anisotropic emission, yields ~43–57% of lunar neutrons in collimation.

LEND measurements are a significant step forward in remote sensing of lunar hydrogen deposits. At low spatial resolution, LEND data demonstrate regional epithermal neutron flux suppression around the poles that increases monotonically toward the pole. Epithermal neutron flux suppression at each pole is the same, implying that hydrogen emplacement at the poles is a regional effect of high latitude. The relative populations of neutrons that contribute to the LEND collimated detectors also demonstrate that a significant fraction of detected neutrons is measured in collimation, which could enable measurements of isolated hydrogen deposits, although that work is not done here. The LEND detectors are more sensitive to fast neutron populations than anticipated, furnishing additional information about hydrogen burial depth.

Mineral hydration was discovered on the Moon's surface around the time of LRO launch. Although these results typically are described as a monolayer, the gradual decrease in epithermal and high-energy epithermal neutron flux with increasing latitude that is measured by LEND is consistent with the degree of hydration suggested by these discoveries if it is assumed that the hydration may extend into the surface by tens of centimeters.

Acknowledgments

TAL was supported by NASA's Lunar Reconnaissance Orbiter project under NASA award number NNG06EO90A to the University of Maryland. RZS and JJS were supported by the LRO project through a cooperative agreement between NASA and the University of Maryland; RDS was supported by a cooperative agreement between NASA and the Catholic University of America; WVB was supported by contract to the University of Arizona; and LGE as supported by contract to the Computer Science Corporation. The Russian co-authors of this paper (IGM, MLL, ABS) were supported by grant No. 14-22-00249 of the Russian Scientific Foundation. The Russian Federal Space Agency supplied the LEND instrument to NASA and the LRO project. The authors would like to thank D. J. Lawrence of the Johns Hopkins University Applied Physics Laboratory for assistance in

1214 obtaining and interpreting the Lunar Prospector neutron data, and for stimulating
1215 discussions that have contributed to this work.

1216

1217 **References**

1218 Binder, A. B. (1998). Lunar Prospector: Overview. *Science* **281**, 1475–1476, doi:
1219 10.1126/science.281.5382.1475.

1220 Boynton, W. V., G. F. Droege, I. G. Mitrofanov, T. P. McClanahan, A. B. Sanin, M. L.
1221 Litvak, M. Schaffner, G. Chin, L. G. Evans, J. B. Garvin, K. Harshman, A.
1222 Malakhov, G. Milikh, R. Sagdeev, and R. Starr (2012). High Spatial Resolution
1223 Studies of Epithermal Neutron Emission from the Lunar Poles: Constraints on
1224 Hydrogen Mobility. *JGR-Planets* **117**, E00H33 (19 pp), doi: 10.1029/2011JE003979.

1225 Carruba, V., and A. Coradini (1999). Lunar Cold Traps: Effects of Double Shielding.
1226 *Icarus* **142**, 402–413, doi: 10.1006/icar.1999.6192.

1227 Clark, R. N. (2009). Detection of Adsorbed Water and Hydroxyl on the Moon. *Science*
1228 **326**, 562–564, doi: 10.1126/science.1178105.

1229 Eke, V. R., L. F. A. Teodoro, D. J. Lawrence, R. C. Elphic, and W. C. Feldman (2012). A
1230 Quantitative Comparison of Lunar Orbital Neutron Data. *Astrophys. J.* **747**, 6, doi:
1231 10.1088/0004-637X/747/1/6.

1232 Feldman, W. C., K. Ahola, B. L. Barraclough, R. D. Belian, R. K. Black, R. C. Elphic, D.
1233 T. Everett, K. R. Fuller, J. Kroesche, D. J. Lawrence, S. L. Lawson, J. L. Longmire,
1234 S. Maurice, M. C. Miller, T. H. Prettyman, S. A. Storms, and G. W. Thornton (2004).
1235 Gamma-Ray, Neutron, and Alpha-Particle Spectrometers for the Lunar Prospector
1236 mission. *JGR-Planets* **109**, E07S06, doi: 10.1029/2003JE002207.

1237 Feldman, W. C., S. Maurice, D. J. Lawrence, R. C. Little, S. L. Lawson, O. Gasnault, R.
1238 C. Wiens, B. L. Barraclough, R. C. Elphic, T. H. Prettyman, J. T. Steinberg, and A. B.
1239 Binder (2001). Evidence for water ice near the lunar poles. *JGR-Planets* **106**, 23231–
1240 23251, doi: 10.1029/2000JE001444.

1241 Feldman, W. C., D. J. Lawrence, R. C. Elphic, B. L. Barraclough, S. Maurice, I. Genetay,
1242 and A. B. Binder (2000). Polar hydrogen deposits on the Moon. *JGR-Planets* **105**,
1243 4175–4196, doi: 10.1029/1999JE001129.

1244 Feldman, W. C., B. L. Barraclough, K. R. Fuller, D. J. Lawrence, S. Maurice, M. C.
1245 Miller, T. H. Prettyman, and A. B. Binder (1999). The Lunar Prospector gamma-ray
1246 and neutron spectrometers. *Nuclear Instruments and Methods in Physical Research,*
1247 *Section A* **422**, 562–566, doi: 10.1016/S0168-9002(98)00934-6.

1248 Feldman, W. C., B. L. Barraclough, S. Maurice, R. C. Elphic, D. J. Lawrence, D. R.
1249 Thomsen, and A. B. Binder (1998a). Major Compositional Units of the Moon: Lunar
1250 Prospector Thermal and Fast Neutrons. *Science* **281**, 1489–1493, doi:
1251 10.1126/science.281.5382.1489.

1252 Feldman, W. C., S. Maurice, A. B. Binder, B. L. Barraclough, R. C. Elphic, and D. J.
1253 Lawrence (1998b). Fluxes of Fast and Epithermal Neutrons from Lunar Prospector:
1254 Evidence for Water Ice at the Lunar Poles. *Science* **281**, 1496–1500, doi:
1255 10.1126/science.281.5382.1496.

1256 Goldstein, D. B., R. S. Nerem, E. S. Barker, J. V. Austin, A. B. Binder, and W. C.
1257 Feldman (1999). Impacting Lunar Prospector in a cold trap to detect water ice.
1258 *Geophys. Res. Lett.* **26**, 1653–1656, doi: 10.1029/1999GL900384.

1259 Hendrix, A. R., K. D. Retherford, G. R. Gladstone, D. M. Hurley, P. D. Feldman, A. F.
1260 Egan, D. E. Kaufmann, P. F. Miles, J. W. Parker, D. Horvath, P. M. Rojas, M. H.
1261 Versteeg, M. W. Davis, T. K. Greathouse, J. Mukherjee, A. J. Steffl, W. R. Pryor, and
1262 S. A. Stern (2012). The lunar far-UV albedo: Indicator of hydration and weathering.
1263 *JGR-Planets* **117**, E12001 (8 pp), doi: 10.1029/2012JE004252.

1264 Hubbard, G. S., A. B. Binder, and W. Feldman (1998). The Lunar Prospector Discovery
1265 Mission: mission and measurement description. *IEEE Transactions on Nuclear*
1266 *Science* **45**, 880–887, doi: 10.1109/23.682655.

1267 Hurley, D. M., G. R. Gladstone, S. A. Stern, K. D. Retherford, P. D. Feldman, W. Pryor,
1268 A. F. Egan, T. K. Greathouse, D. E. Kaufmann, A. J. Steffl, J. W. Parker, P. F. Miles,
1269 D. Horvath, M. W. Davis, M. H. Versteeg, D. C. Slater, A. R. Hendrix, C. A.
1270 Hibbitts, C. M. Ernst, R. J. Vervack, Jr., and G. A. Grieves (2012). Modeling of the
1271 vapor release from the LCROSS impact: 2. Observations from LAMP. *JGR-Planets*
1272 **117**, E00H07, doi: 10.1029/2011JE003841.

1273 Lawrence, D. J., V. R. Eke, R. C. Elphic, W. C. Feldman, H. O. Funsten, T. H.
1274 Prettyman, and L. F. A. Teodoro (2011a). Technical Comment on "Hydrogen
1275 Mapping of the Lunar South Pole Using the LRO Neutron Detector Experiment
1276 LEND". *Science* **334**, 1058, doi: 10.1126/science.1203341.

1277 Lawrence, D. J., D. M. Hurley, W. C. Feldman, R. C. Elphic, S. Maurice, R. S. Miller,
1278 and T. H. Prettyman (2011b). Sensitivity of orbital neutron measurements to the
1279 thickness and abundance of surficial lunar water. *JGR-Planets* **116**, E01002, doi:
1280 10.1029/2010JE003678.

1281 Lawrence, D. J., R. C. Elphic, W. C. Feldman, H. O. Funsten, and T. H. Prettyman
1282 (2010). Performance of Orbital Neutron Instruments for Spatially Resolved Hydrogen
1283 Measurements of Airless Planetary Bodies. *Astrobiology* **10**, 183–200, doi:

10.1089/ast.2009.0401.

Lawrence, D. J., W. C. Feldman, R. C. Elphic, J. J. Hagerty, S. Maurice, G. W. McKinney, and T. H. Prettyman (2006). Improved modeling of Lunar Prospector neutron spectrometer data: Implications for hydrogen deposits at the lunar poles. *JGR-Planets* **111**, E08001, doi: 10.1029/2005JE002637.

Little, R. C., W. C. Feldman, S. Maurice, I. Genetay, D. J. Lawrence, S. L. Lawson, O. Gasnault, B. L. Barraclough, R. C. Elphic, T. H. Prettyman, and A. B. Binder (2003). Latitude variation of the subsurface lunar temperature: Lunar Prospector thermal neutrons. *JGR-Planets* **108**, 5046–5054, doi: 10.1029/2001JE001497.

Litvak, M. L., I. G. Mitrofanov, A. B. Sanin, D. V. Golovin, A. V. Malakhov, W. V. Boynton, G. F. Droege, K. Harshman, and R. D. Starr (2012a). LEND neutron data processing for the mapping of the Moon. *JGR-Planets* **117**, E00H32 (21 pp), doi: 10.1029/2011JE004035.

Litvak, M. L., I. G. Mitrofanov, A. Sanin, A. Malakhov, W. V. Boynton, G. Chin, G. Droege, L. G. Evans, J. Garvin, D. V. Golovin, K. Harshman, T. P. McClanahan, M. I. Mokrousov, E. Mazarico, G. Milikh, G. Neumann, R. Sagdeev, D. E. Smith, R. Starr, and M. T. Zuber (2012b). Global maps of lunar neutron fluxes from the LEND instrument. *JGR-Planets* **117**, E00H22 (18pp), doi: 10.1029/2011JE003949.

Litvak, M. L., I. G. Mitrofanov, A. B. Sanin, B. N. Bakhtin, J. G. Bodnarik, W. V. Boynton, G. Chin, L. G. Evans, K. Harshman, T. A. Livengood, A. Malakhov, M. I. Mokrousov, T. P. McClanahan, R. Sagdeev, and R. Starr (2016). The variations of neutron component of lunar radiation background from LEND/LRO observations. *Planet. & Space Sci.* **122**, 53–65, doi: 10.1016/j.pss.2016.01.006.

Livengood, T. A., G. Chin, R. Z. Sagdeev, I. G. Mitrofanov, W. V. Boynton, Evans, L. G., M. L. Litvak, T. P. McClanahan, A. B. Sanin, R. D. Starr, and J. J. Su (2015). Moonshine: Diurnally varying hydration through natural distillation on the Moon, detected by the Lunar Exploration Neutron Detector (LEND). *Icarus* **255**, 100–115, doi: 10.1016/j.icarus.2015.04.004.

Livengood, T. A., L. D. Deming, M. F. A'Hearn, D. Charbonneau, T. Hewagama, C. M. Lisse, L. A. McFadden, V. S. Meadows, T. D. Robinson, S. Seager, and D. D. Wellnitz (2011). Properties of an Earth-Like Planet Orbiting a Sun-Like Star: Earth Observed by the EPOXI Mission. *Astrobiology* **11**, 907–930, doi: 10.1089/ast.2011.0614.

Maurice, S., D. J. Lawrence, W. C. Feldman, R. C. Elphic, and O. Gasnault (2004). Reduction of neutron data from Lunar Prospector. *JGR-Planets* **109**, E07S04 (40pp), doi: 10.1029/2003JE002208.

1320 Maurice, S., W. C. Feldman, D. J. Lawrence, R. C. Elphic, O. Gasnault, C. d'Uston, I.
1321 Genetay, and P. G. Lucey (2000). High-energy neutrons from the Moon. *JGR-Planets*
1322 **105**, E8, 20365–20376, doi: 10.1029/1999JE001151.

1323 Mazarico, E., G. A. Neumann, D. E. Smith, M. T. Zuber, and M. H. Torrence (2011).
1324 Illumination conditions of the lunar polar regions using LOLA topography. *Icarus*
1325 **211**, 1066–1081, doi: 10.1016/j.icarus.2010.10.030.

1326 McElhaney, S. A., M. L. Bauer, M. M. Chiles, M. B. Emmett, and J. H. Todd (1990).
1327 Monte Carlo and experimental evaluation of BC-454 for use as a multienergy neutron
1328 detector. *IEEE Transactions on Nuclear Science* **37**, 1351–1358.

1329 Miller, R. S., G. Nerurkar, and D. J. Lawrence (2012). Enhanced Hydrogen at the Lunar
1330 Poles: New Insights From the Detection of Epithermal and Fast Neutron Signatures.
1331 *JGR-Planets* **117**, E11007 (11012 pp), doi: 10.1029/2012JE004112.

1332 Mitrofanov, I. G., W. V. Boynton, M. L. Litvak, A. B. Sanin, and R. D. Starr (2011).
1333 Response to Comment on "Hydrogen Mapping of the Lunar South Pole Using the
1334 LRO Neutron Detector Experiment LEND". *Science* **334**, 1058-d, doi:
1335 10.1126/science.1203483.

1336 Mitrofanov, I. G., A. Bartels, Y. I. Bobrovnitsky, W. Boynton, G. Chin, H. Enos, L.
1337 Evans, S. Floyd, J. Garvin, D. V. Golovin, A. S. Grebennikov, K. Harshman, L. L.
1338 Kazakov, J. Keller, A. A. Konovalov, A. S. Kozyrev, A. R. Krylov, M. L. Litvak, A.
1339 V. Malakhov, T. McClanahan, G. M. Milikh, M. I. Mokrousov, S. Ponomareva, R. Z.
1340 Sagdeev, A. B. Sanin, V. V. Shevchenko, V. N. Shvetsov, R. Starr, G. N.
1341 Timoshenko, T. M. Tomilina, V. I. Tretyakov, J. Trombka, V. S. Troshin, V. N.
1342 Uvarov, A. B. Varenikov, and A. A. Vostrukhin (2010a). Lunar Exploration Neutron
1343 Detector for the NASA Lunar Reconnaissance Orbiter. *Space Science Reviews* **150**,
1344 183–207, doi: 10.1007/s11214-009-9608-4.

1345 Mitrofanov, I. G., A. B. Sanin, W. V. Boynton, G. Chin, J. B. Garvin, D. Golovin, L. G.
1346 Evans, K. Harshman, A. S. Kozyrev, M. L. Litvak, A. Malakhov, E. Mazarico, T.
1347 McClanahan, G. Milikh, M. Mokrousov, G. Nandikotkur, G. A. Neumann, I.
1348 Nuzhdin, R. Sagdeev, V. Shevchenko, V. Shvetsov, D. E. Smith, R. Starr, V. I.
1349 Tretyakov, J. Trombka, D. Usikov, A. Varenikov, A. Vostrukhin, and M. T. Zuber
1350 (2010b). Hydrogen Mapping of the Lunar South Pole Using the LRO Neutron
1351 Detector Experiment LEND. *Science* **330**, 483–486, doi: 10.1126/science.1185696.

1352 Pieters, C. M., J. N. Goswami, R. N. Clark, M. Annadurai, J. Boardman, B. Buratti, J.-P.
1353 Combe, M. D. Dyar, R. Green, J. W. Head, C. Hibbitts, M. Hicks, P. Isaacson, R.
1354 Klima, G. Kramer, S. Kumar, E. Livo, S. Lundeen, E. Malaret, T. McCord, J.
1355 Mustard, J. Nettles, N. Petro, C. Runyon, M. Staid, J. Sunshine, L. A. Taylor, S.
1356 Tompkins, and P. Varanasi (2009). Character and Spatial Distribution of OH/H2O on

1357 the Surface of the Moon Seen by M3 on Chandrayaan-1. *Science* **326**, 568–582, doi:
1358 10.1126/science.1178658.

1359 Press, W. H., B. P. Flannery, S. A. Teukolsky, and W. T. Vetterling (1989), *Numerical*
1360 *Recipes in Pascal: The Art of Scientific Computing*, 759 pp., Cambridge University
1361 Press, New York.

1362 Sanin, A. B., I. G. Mitrofanov, M. L. Litvak, A. Malakhov, W. V. Boynton, G. Chin, G.
1363 Droege, L. G. Evans, J. Garvin, D. V. Golovin, K. Harshman, T. P. McClanahan, M.
1364 I. Mokrousov, E. Mazarico, G. Milikh, G. Neumann, R. Sagdeev, D. E. Smith, R. D.
1365 Starr, and M. T. Zuber (2012). Testing lunar permanently shadowed regions for water
1366 ice: LEND results from LRO. *JGR-Planets* **117**, E00H26, doi:
1367 10.1029/2011JE003971.

1368 Starukhina, L. V., and Y. G. Shkuratov (2000). NOTE: The Lunar Poles: Water Ice or
1369 Chemically Trapped Hydrogen? *Icarus* **147**, 585–587, doi: 10.1006/icar.2000.6476.

1370 Sunshine, J. M., T. L. Farnham, L. M. Feaga, O. Groussin, F. Merlin, R. E. Milliken, and
1371 M. F. A'Hearn (2009). Temporal and Spatial Variability of Lunar Hydration As
1372 Observed by the Deep Impact Spacecraft. *Science* **326**, 565–568, doi:
1373 10.1126/science.1179788.

1374 Teodoro, L. F. A., V. R. Eke, and R. C. Elphic (2010). Spatial distribution of lunar polar
1375 hydrogen deposits after KAGUYA (SELENE). *Geophys. Res. Lett.* **37**, L12201, doi:
1376 10.1029/2010GL042889.

1377 Teodoro, L. F. A., V. R. Eke, R. C. Elphic, W. C. Feldman, and D. J. Lawrence (2014).
1378 How well do we know the polar hydrogen distribution on the Moon? *JGR-Planets*
1379 **119**, 574–593, doi: 10.1002/2013JE004421.

1380 Watson, K., B. C. Murray, and H. Brown (1961). The behavior of volatiles on the lunar
1381 surface. *J. Geophys. Res.* **66**, 3033–3045, doi: 10.1029/JZ066i009p03033.

1382 Vasavada, A. R., J. L. Bandfield, B. T. Greenhagen, P. O. Hayne, M. A. Siegler, J.-P.
1383 Williams, and D. A. Paige (2012). Lunar equatorial surface temperatures and regolith
1384 properties from the Diviner Lunar Radiometer Experiment. *JGR-Planets* **117**,
1385 E00H18 (12 pp), doi: 10.1029/2011JE003987.

1386 Vondrak, R. R. (2012). Introduction to special section on Results of the Lunar
1387 Reconnaissance Orbiter Mission. *JGR-Planets* **117**, E00H01 (03 pp), doi:
1388 10.1029/2012JE004298.

1389

Table 1: LEND detector maps modeled using LP maps alone

	LEND STN3	LEND SETN	LEND CSETN
Mean count rate	24.93±0.02 cps	10.622±0.002 cps	5.082±0.001 cps
uniform count rate component	0.0±1.0 cps (0±4%)	0.4±0.9 cps (4±8%)	2.9±0.3 cps (57±6%)
count rate due to LP thermal component	8.4±0.4 cps (34±2%)	0.3±0.1 cps (3±1%)	0.00±0.02 cps (0.0±0.3%)
count rate due to LP epithermal component	12.4±1.4 cps (49±5%)	8.0±0.8 cps (75±8%)	1.0±0.2 cps (19±5%)
count rate due to LP fast neutron component	4.2±1.1 cps (17±4%)	1.9±0.5 cps (18±5%)	1.2±0.1 cps (24±2%)
variance	0.0932	0.01500	0.002058

Table 2: LEND detector maps modeled using a combination of LP and LEND maps

	LEND STN3	LEND SETN	LEND CSETN
Mean count rate	24.93±0.02 cps	10.622±0.002 cps	5.082±0.001 cps
uniform count rate component	1.12 cps (4.5%)	0.77 cps (7%)	2.90±0.23 cps (57±4%)
count rate due to LP thermal component	7.54±0.11 cps (30.3±0.4%)		
count rate due to STN3-thermal component[a]		0.35±0.14 cps (3±1%)	0.00±0.02 cps (0.0±0.3%)
count rate due to LP epithermal component		7.61±0.54 cps (72±5%)	
count rate due to SETN-epithermal component[b]	16.26±0.12 cps (65.2±0.5%)		1.18±0.21 cps (23±4%)
count rate due to LP fast neutron component		1.89±0.42 cps (18±4%)	1.00±0.10 cps (20±2%)
variance	0.0395	0.01472	0.001813
# degrees of freedom	7200 – 2	7200 – 3	7200 – 4
ratio of variances (F)	2.36	1.019	1.135
confidence of F[c]	100%	79%	100%

[a] For fitting SETN and CSETN detectors, STN3-thermal component = STN3 – 1.651•(SETN – 0.77) – 1.12 cps.

[b] For fitting STN3 detector, SETN-epithermal component = SETN – 0.77 cps; for fitting CSETN detector, SETN-epithermal component = SETN – 0.047•STN3-thermal – 0.77 cps.

[c] confidence of F = confidence that the ratio of fit variances is statistically distinguishable.

Table 3: Estimated LEND data-reduction coefficients

	LEND STN3	LEND SETN	LEND CSETN
Mean count rate	24.93±0.02 cps	10.622±0.002 cps	5.082±0.001 cps
uniform count rate component	1.12 cps	0.77 cps	2.90±0.23 cps
coefficient of STN3-thermal component		0.047±0.019 • (STN3 – 1.12 – 1.651±0.012 • (SETN – 0.77))	
coefficient of SETN epithermal component	1.651±0.012 • (SETN – 0.77)		

Table 4: LEND individual collimated detector maps, modeled using a combination of LP and LEND maps

	CSETN1 (cps)	CSETN2 (cps)	CSETN3 (cps)	CSETN4 (cps)	Sum of CSETNx (cps)
Mean count rate	1.1302 ± 0.0002	1.3087 ± 0.0003	1.2536 ± 0.0003	1.3758 ± 0.0003	5.0683 ± 0.0006
uniform component	0.67±0.09	0.79±0.11	0.71±0.12	0.79±0.11	2.96±0.21
STN3_thermal component [a]	0±0.01	0±0.01	0±0.01	0±0.01	0.00±0.03
SETN_epithermal component [b]	0.24±0.09	0.27±0.11	0.32±0.11	0.33±0.09	1.17±0.21
LP fast neutron component	0.22±0.05	0.25±0.06	0.22±0.07	0.25±0.06	0.95±0.12
for combined CSETN, scale by	0.527 / 0.460 = 1.146	0.527 / 0.520 = 1.013	0.527 / 0.541 = 0.974	0.527 / 0.589 = 0.895	

[a] STN3_thermal component = STN3 – 1.651•(SETN – 0.77) – 1.12 cps.

[b] SETN_epithermal component = SETN – 0.047•STN3_thermal – 0.77 cps.

Table 5: Neutron flux suppression at the lunar poles, within 10°

	Equator, ±10°	North pole, 80°–90°			South pole, 80°–90°S		
	Neutron count rate	Neutron count rate	% Equator[c]	wt% WEH[d]	Neutron count rate	% Equator[c]	wt% WEH[d]
LP thermal neutrons			110.8±0.2			114.8±0.2	
STN3 signal	24.911 ±0.002	24.655 ±0.003	98.97 ±0.01		25.065 ±0.003	100.62 ±0.01	
STN3 Thermal[a]	7.31 ± 0.11	7.81 ± 0.11	106.9±0.1		8.11 ± 0.11	111.0±0.2	
LP epithermal			98.38 ±0.04	0.031 ±0.001		98.18 ±0.04	0.035 ±0.001
LP fast			95.74 ±0.06	0.085 ±0.001		96.01 ±0.05	0.079 0.001
SETN signal	10.752 ±0.002	10.283 ±0.002	95.64 ±0.03	0.0871 ±0.0005	10.353 ±0.002	96.29 ±0.03	0.0736 ±0.0005
SETN Epithermal[a]	9.68±0.13	9.20±0.13	95.0±0.1	0.100 ±0.001	9.25±0.13	95.6±0.1	0.088 ±0.001
CSETN signal	5.113 ±0.001	5.001 ±0.002	97.81 ±0.04	0.043 ±0.001	5.005 ±0.002	97.89 ±0.04	0.041 ±0.001
CSETN HEE[b]	2.21±0.23	2.10±0.23	95.0±0.6	0.10±0.01	2.11±0.23	95.5±0.5	0.09±0.01

[a] Estimated background per this work, Table 2, uncertainty in thermal component since uniform component has fixed value and uncertainties in epithermal and fast components are covariant.

[b] Estimated background per this work, Table 2, uncertainty in subtracted uniform component since uncertainties in epithermal and fast components are covariant.

[c] Polar signal as percentage of equatorial signal. Uncertainty estimated from population statistics of adding/subtracting covariant uncertainty equally to polar and equatorial signal measurement.

[d] Weight-percent water-equivalent hydrogen (WEH), calibration estimated from Fig. 1 of Mitrofanov *et al.* (2010a), as wt% = $1.91 \bullet (C_0/C_1 - 1)$.

1425 Table 6: Neutron flux suppression at the lunar poles, within 2°

	Equator, ±2°	North pole, 88°–90°			South pole, 88°–90°S		
	Neutron count rate	Neutron count rate	% Equator[c]	wt% WEH[d]	Neutron count rate	% Equator[c]	wt% WEH[d]
LP thermal neutrons			110.7±0.4			117.9±0.4	
STN3 signal	24.883 ±0.006	24.436 ±0.008	98.20 ±0.04		25.012 ±0.008	100.52 ±0.04	
STN3 Thermal[a]	7.27 ± 0.11	7.84 ± 0.11	108.3±0.1		8.29 ± 0.11	114.4±0.2	
LP epithermal			97.3±0.1	0.054 ±0.002		96.9±0.1	0.061 ±0.002
LP fast			95.3±0.1	0.095 ±0.003		94.4±0.1	0.113 0.002
SETN signal	10.755 ±0.004	10.147 ±0.005	94.4±0.1	0.113 ±0.002	10.211 ±0.005	94.9±0.1	0.103 ±0.002
SETN Epithermal[a]	9.69±0.13	9.05±0.13	93.6±0.1	0.130 ±0.002	9.10±0.13	94.1±0.1	0.120 ±0.002
CSETN signal	5.120 ±0.003	4.981 ±0.004	97.3±0.1	0.053 ±0.002	4.985 ±0.004	97.4±0.1	0.051 ±0.002
CSETN HEE[b]	2.22±0.23	2.08±0.23	93.7±0.7	0.13±0.02	2.09±0.23	94.1±0.7	0.12±0.02

1426 [a] Estimated background per this work, Table 2, uncertainty in thermal component since
1427 uniform component has fixed value and uncertainties in epithermal and fast
1428 components are covariant.

1429 [b] Estimated background per this work, Table 2, uncertainty in subtracted uniform
1430 component since uncertainties in epithermal and fast components are covariant.

1431 [c] Polar signal as percentage of equatorial signal. Uncertainty estimated from population
1432 statistics of adding/subtracting covariant uncertainty equally to polar and equatorial
1433 signal measurement.

1434 [d] Weight-percent water-equivalent hydrogen (WEH), calibration estimated from Fig. 1
1435 of Mitrofanov *et al.* (2010a), as wt% = $1.91 \bullet (C_0/C_1 - 1)$.

1436